The Pennsylvania State University

The Graduate School

NUMERCIAL SIMULATION OF PROPPANT DISPLACEMENT IN SCALED FRACTURE NETWORKS

A Thesis in

Energy and Mineral Engineering

by

Yibo Song

© 2020 Yibo Song

Submitted in Partial Fulfillment
of the Requirements
for the Degree of

Master of Science

August 2020

The thesis of Yibo Song was reviewed and approved by the following:

Arash Dahi Taleghani
Associate Professor of Petroleum and Natural Gas Engineering
Thesis Advisor

Gregory R. King
Professor of Practice of Petroleum and Natural Gas Engineering

John Yilin Wang
Associate Professor of Petroleum and Natural Gas Engineering

Mort D. Webster
Professor of Energy Engineering
Associate Department Head for Graduate Education

ABSTRACT

While hydraulic fracturing is recognized as the most effective stimulation technique for unconventional reservoirs, the production enhancement is influenced by several factors including proppant placement inside the fractures. The goal of this work is to understand the proppant transport and its placement process in “T” shaped fracture network through simulations. The proppant transport is studied numerically by coupling a computational fluid dynamic model for the base shear-thinning fluid and the discrete element methods for proppant particles. In the CFD model, the forces on proppants are calculated based on fluid properties, while fluid properties are updated based on the particle concentration at any point and time. In the DEM model, the motion and position of each individual proppant is calculated based on the gravity and drag forces from the CFD model, which makes it possible to reproduce some phenomena that cannot be simulated in continuum concentration-oriented models. A scaling analysis has been performed to scale down the model from field scale to lab scale by deriving relevant dimensionless variables. Different proppant size distributions and injection velocities are considered, as well as the friction and cohesion effects among particle and fracture surface. The simulation results show that in the primary fracture, the injected proppants could divide into three layers: the bottom sand bed zone, the middle surface rolling zone, and the top slurry flow zone. The total number of the proppants do not increase much after the sand dune reach an equilibrium height. A smaller size proppant would benefit the development of sand dune in the secondary fracture, whereas a larger proppant size would benefit the increase rate of the sand dune. The equilibrium height of sand dune in the minor fracture could be greater than the primary fracture, and the distribution of proppant dunes is symmetric. A lower proppant load would amplify the impact of friction as well as the erosion force, which would finally deliver a negative impact on equilibrium height. Two deposit mechanisms have also identified in the bypass fracture network.

TABLE OF CONTENTS

LIST OF FIGURES v

LIST OF TABLES vii

ACKNOWLEDGEMENTS viii

Chapter 1 Introduction 1

Chapter 2 Methodology 5

Chapter 3 Scaling Analysis 11

Chapter 4 Results and Discussions 17

- Case 1: Planar Fracture Case 17
- Case 2: T-Shaped Fracture Case 24
- Case 3: Verification of Scaling Strategy 32
- Case 4: Impact of the Bypass Fracture 37
- Case 5: Impact of Proppant Concentration 42
- Case 6: Impact of Proppant Mesh Size 45
- Case 7: Impact of Injection Velocity 47

Chapter 5 Conclusions 53

References 55

Appendix Scaling Analysis via Ipsen's Method 59

LIST OF FIGURES

Figure **2-1**: Calculation cycle of CFD-DEM coupling model 10

Figure **4-1**: The geometry of the model and mesh of Case *1* 19

Figure **4-2**: Proppant distribution at an earlier stage of Case *1* 20

Figure 4-3: Comparison of proppant deposition and transport between simulation result and lab experiment results by Kera et al. (1956) 21

Figure **4-4**: Final distribution of proppants in Case *1* 22

Figure **4-5**: Comparison of simulation result and lab experiment result of Case *1* 22

Figure **4-6**: Interaction between fluid and particles in Case *1* 23

Figure **4-7**: Pressure difference between inlet and outlet in Case *1* 24

Figure **4-8**: The geometry of the model and mesh of Case *2* 25

Figure **4-9**: Proppant distribution of Case *2* after injecting *8.93* primary fracture volumes of proppant slurry 26

Figure **4-10**: Proppant distribution of Case *2* after injecting *33* primary fracture volumes of proppant slurry 27

Figure **4-11**: Proppant distribution in fracture network of Case *2* 28

Figure **4-12**: Proppant flow zone in primary fracture of Case *2* 28

Figure **4-13**: Number of proppants in fracture during the simulation in Case *2* 29

Figure **4-14**: Interaction between fluid and particles in Case *2* 30

Figure **4-15**: Proppant distribution in the primary fracture of Case *2* with 1.5 times longer distance of the intersection point from injection well 31

Figure **4-16**: Comparison of proppant distribution in primary fracture of Case *2* and Case *3* 33

Figure **4-17**: Comparison of proppant distribution in secondary fracture of Case 2 and Case *3* 34

Figure **4-18**: Number of proppants in fracture during the simulation of Case *3* 35

Figure **4-19**: Schematic Diagram of T*2* Slot 36

Figure **4-20**: Comparison of simulation result and lab experiment result of primary fracture 37

Figure **4-21**: Comparison of simulation result and lab experiment result of secondary fracture 37

Figure **4-22**: Proppant distribution in the primary fracture of Case *4* 39

Figure **4-23**: Proppant distribution in the bypass Fracture of Case *4* 39

Figure **4-24**: Outflow velocity of Case *4* 40

Figure **4-25**: Comparison of deposit mechanism of proppant in bypass fracture.....41

Figure **4-26**: Interaction between fluid and particles of Case *4*.....42

Figure **4-27**: Proppant distribution in fracture network of Case *5* with lower concentration...44

Figure **4-28**: Proppant distribution in fracture network of Case *5* with higher concentration 45

Figure **4-29**: Proppant distribution in fracture network of Case *6*.....47

Figure **4-30**: Proppant distribution after injecting *7.96* primary fracture volumes proppant slurry of Case *7* with injection rate as *0.22 m/*s.....48

Figure **4-31**: Proppant distribution after injecting *69.25* primary fracture volumes proppant slurry of Case *7* with injection rate as *0.22 m/*s.....50

Figure **4-32**: Proppant distribution of Case *7* with injection rate as *0.44 m/s* 51

LIST OF TABLES

Table 4-1: Fracture dimensions and properties 18

Table 4-2: Particle Properties 19

Table 4-3: List of dimensions for the filed reference fracture and the simulation model of Case *2* 25

Table 4-4: Comparison of dimensions among Case *2* and Case *3* 32

ACKNOWLEDGEMENTS

First of all, I would like to express my sincere gratitude to my thesis advisor Dr. Arash Dahi Taleghani, for his continuous support on my master's study. I'm inspired not only by his research method but also by his academic attitude. He is not only my academic advisor but also my mentor, my friend. I'm pretty sure what he told me here would benefit my entire life. I will remember what he has taught me, and I hope there's a day he would be proud of me.

I would also like to thank Dr. John Yilin Wang and Dr. Gregory King, to serve as my committee member. I still remember when I first started this research, it is Dr. Wang's course that equips me with the detailed knowledge and helps me to move further.

My sincere thank also goes to my senior sister Yuzhe Cai and my close brother Lu Lee for their tremendous help on my research and personal life. I am then extending my thanks to Dr. Long Fan, my dearest sisters Rui Liu and Chengcheng Lu.

Also, thank my lovely friends, Fangya Niu and Jiayi Fan, for their friendship, support, encouragement, and understanding. Words cannot express how important they are in my life. Without them, I won't have an experience as colorful as what I have now.

I want to thank Zhiyuan Li for his care, trust, company, tolerance, and understanding. He makes me be a better person. Even though we sometimes argue with each other, we are still great accompanies and we learn from each other. Without him, I won't be that happy. Without him, I won't keep fighting when I want to give up. Thanks, my man.

Last, I would like to thank my family, my brothers and my parents. They always trust me and support me. They are the best families in the world. I also send my special gratitude to my grandparents, who give their purest love to me. I still miss them, and I always hoped they were watching from somewhere above. I hope they would be proud of their beloved grandson if they see the fantastic job he has done in this amazing journey.

Chapter 1

Introduction

Within recent decades, unconventional oil and gas resources locked in shales and tight sand formations is becoming an essential component source in the oil and gas industry. New advanced technologies continuously introduced into the industry to enhance the efficiency and recovery rate. Among those new techniques, hydraulic fracturing has been applied regularly as a stimulation treatment. The induced fractures usually provide a higher hydraulic conductivity, which leads to an increment of Stimulated Reservoir Volume (SRV) and consequently improvement of production performance. Proppants are indispensable in hydraulic fractures to maintain the required aperture for the fracture network to flow (Britt *et al*., 2006). The overall fracture conductivity depends on the distribution of proppants inside the fractures. Moreover, the productivity of a fractured well depends on the propped fracture length. Thus, to better understand the hydraulic fracturing process and enhance the performance of hydraulic fractures, there has been efforts on studying proppant transport in the past decades. The first published laboratory experiment on proppant transport is presented by Kern *et al.* (1959). They studied the transport of sand within the slot flow. They use regular water as fracturing fluid and sand as proppants. The slot was formed by two parallel Plexiglas sheets, this configuration is still used to run similar experiments. Through the transport process, the sands hold a trend to settle down as soon as they flow inside the fracture slot. Then the settled sands formed a sand bed that soon developed to a dune. The dune further grows with time until it reaches a constant height. Their study also indicates that proppant injected early settles down near the entrance and the later injected proppants flow further in-depth into the fracture. The flowing experimental studies by Barree and Conway (1995) obtained results similar to Kern *et al.* (1956). Brannon *et al.* (2006) extend this experiment into a larger scale with a 16 ft long, 22 in high

slot. By study the effects of fracturing fluid additives as well as proppant transport capability, they determined the impact of fracturing fluid on proppant transport process.

Wang *et al.* (2003) introduce a bi-power law by correlation of proppant and fluid Reynolds number with logarithmic functions of dimensionless sedimentation numbers. They come up with a three-zone proppant flow model following the experimental observations. Gadde *et al.*(2004) conduct an experiment for proppant transport within a slot with rough surfaces. Based on their results, they proposed a correlation for proppant flow which include the fracture width, proppant size, proppant load and fluid rheology. Liu and Sharma (2005) studied the impact of fracture width and fluid rheology. They concluded that the impact of fracture width is depending on the proppant diameter.

Sierra *et al.* (2014) introduce a 90° secondary fracture into the experiment. The proppant pump into the primary slot then flow into the secondary fracture. Trough the experiment, they conduct a pumping rate threshold. Proppant would roll into the secondary fracture through the surface of the sand bed rather than flow into the secondary fracture with a pumping rate under the threshold. Sahai *et al.* (2014) done another comprehensive experiment to study proppant transport in complex fracture networks. They compared their laboratory result with simulation results obtained by Wang *et al.*(2003) and determined that the pump rate has a major impact on proppant transport and settling in fracture network. Alotaibi and Miskimins (2015) finished another related experiment work and discuss the mechanism of proppant transport based on the experiment results.

Tong and Mohanty (2016) conduct both experiment and simulation on proppant transport in fracture networks. To present fracture networks, they use fracture slot with different bypass angles in experiment and a “T” shape geometry model in numerical model. Based on the results they obtained, they divide the transport zone into 3 part: bottom immobile sand bed zone, middle flowing slurry zone and top clear fluid zone. They also discussed the effect of the fluid shear rate.

The entrance eroded region and sand bed length will increase with shear rate, whereas equilibrium sand bed height will decrease.

Recently, numerical simulation works also performed to study the impact of production activities on proppant distribution. Zhang *et al.* (2017) build a 2D numerical model to study proppant transport and distribution in hydraulic fractures. They focus on horizontal wells and conduct that over flushing process with a high flushing rate would generate a large proppant-free region. In the same year, Zhang *et al.*(2017) use the same method study proppant the transport and placement of multi-sized proppants in hydraulic fracture. They relate the proppant transport mechanism with the vortex based on their simulation results. Proppant particles would transport to different locations in the fracture due to the drag force from the vortex, which finally lead to a dual-dune profile.

Previous studies about proppant transport include both lab experiments and numerical simulations. The lab experiments are usually implemented in a slot to represent hydraulic fractures. Different sizes and concentrations of proppant can always be incorporated in such experiments, but these experiments are usually conducted at very low pressure and low pressure-gradient environments. The numerical simulations are mainly performed by solving Navier-Stokes via Computational Fluid Dynamics (CFD). In recent decades, a combination of CFD and DEM methods becomes a more popular method to solve proppant transport problems. Discrete element methods (DEM) is a typical simulation method to model particulate materials in a discretized form. Within the study of proppant transport, the behavior of proppant particles can be comprehensively studied via DEM. However, in previous studies, when introducing the concept of DEM into the CFD model, the DEM is usually treated as a supplementary of CFD. As a result, although the existed models, such as the model used by Tong and Mohanty (2016), can model the particle phase. The particle phase remains as continuous as the fluid phase. Then an apparent separation between the results obtained by lab experiments and numerical simulations can be observed. Also, the

interactions between particles cannot be clearly identified via the existing continuous models. These essential differences result in a limited understanding of proppant transport misleading results that ended in poor hydraulic fracturing treatment designs.

In this study, a coupled CFD and DEM simulation has been adopted to model proppant transport. However, interactions between these two components play a critical role in the physical phenomena involved in this process. The interactions between particles can be clearly observed in the simulation results. Based on published experimental data, several simulations have been conducted to study proppant displacement and distribution in hydraulic fractures.

Chapter 2

Methodology

Different from the continuum modeling approach, the discrete approach could model every single particle in the model, which means interactions between all individual particles from the behavior of the overall system. There are two approaches to discrete simulation. One approach is the hard-sphere model, which treats interaction forces between particles as impulsive. Another approach is the soft-sphere model, which is applied in the simulation due to the relatively high accuracy. In this model, particles are assumed rigid, small overlaps are introduced to represent the deformation through collision. The post-collision velocities are calculated by simplified force laws.

DEM analysis consists of two parts: One part is determining the force acting on particles by contact detection algorithms as well as contact mechanics models. Another part is determining accelerations, velocities, and positions of particles with force data from part one, by applying Newton's law of motion and numerical integration.

There are two components of the contact model. One is the base model. The most common models include Hertz-Mindlin (no slip), Linear Spring, Hysteretic Spring, Edinburgh elastoplastic adhesion. Another is the rolling fraction model; the most common use models include standard rolling friction, RVD rolling friction. The Hertz-Mindlin (no slip) model, has been introduced into this study as a contact model to determine particle interactions due to its high accuracy and efficiency on force calculation (D.E.M. Solutions, 2018). Within the model, there are two force components need to be clarified. One component is the normal force, which based on Hertzian contact. Another force is the tangential force. In particular, for normal force F_n, is a function of normal overlap δ_n as following (Khan and Bushell, 2005).

$$F_n = \frac{4}{3} E^* \sqrt{R^*} \delta_n{}^{\frac{3}{2}}, \qquad (\mathbf{2-1})$$

where E^* is equivalent Young's Modulus which is defined as

$$\frac{1}{E^*} = \frac{(1-{\nu_i}^2)}{E_i} + \frac{(1-{\nu_j}^2)}{E_j}, \qquad (\mathbf{2-2})$$

$E_{i,}\ E_{j,}\nu_i\ and\ \nu_j$ are Young's Modulus and Poisson ratio of the spheres in contact. R^*, in the above equation, is the equivalent radius which is defined by

$$\frac{1}{R^*} = \frac{1}{R_i} + \frac{1}{R_j}, \qquad (\mathbf{2-3})$$

R_i and R_j are the radius of each sphere in contact. The damping force ${F_n}^d$ is defined as (Sakaguchi *et al.*, 1993)

$${F_n}^d = -2\sqrt{\frac{5}{6}}\beta\sqrt{S_n m^*}{v_n}^{\overrightarrow{rel}}, \qquad (\mathbf{2-4})$$

where $m^* = (\frac{1}{m_1} + \frac{1}{m_i})^{-1}$ is the equivalent mass, ${v_n}^{rel}$ is the normal component of the relative velocity, $S_n = 2\ E^*\sqrt{R^*\delta_n}$ is the normal stiffness, β is a constant. E is the coefficient of restitution. Also, the tangential force F_t depends on the tangential overlap δ_t and tangential stiffness S_t

$$F_t = -S_t\delta_t, \qquad (\mathbf{2-5})$$

with

$$S_t = 8G^*\sqrt{R^*\ \delta_n}\,, \qquad (\mathbf{2-6})$$

where G^* is the equivalent shear modulus. The tangential damping force ${F_t}^d$(Sakaguchi *et al.*, 1993)

$${F_t}^d = -2\sqrt{\frac{5}{6}}\beta\sqrt{S_t m^*}{v_t}^{\overrightarrow{rel}}\,, \qquad (\mathbf{2-7})$$

where ${v_t}^{rel}$ is the tangential component of the relative velocity.

The tangential force is also limited by Coulomb friction $\mu_s F_n$, with the coefficient of static friction μ_s.

In the DEM simulation, each particle has two types of motion: rotation and translation. By using Newton's second law, both rotation and translation accelerations (6 components for each particle) can be calculated. Then based on the acceleration results, the velocities and positions can be updated by numerically integrated over a time step.

The motion of particles is calculated by the following equations. Equation 8 shows the calculation process for rotation

$$I\frac{d\omega}{dt} = \Pi\,, \qquad (\mathbf{2-8})$$

where I is the moment of inertia, ω is the angular velocity, t is time, Π is the resultant contact torque acting on the particle.

Equation 2-9 shows the calculation process for translation

$$m\frac{dv}{dt} = F_g + F_c + F_{nc}, \qquad (\mathbf{2-9})$$

where m is the mass of the particle, v is the translational velocity of the particle, t is time, F_g is the resultant gravitational force acting on the particle and F_c and F_{nc} are the resultant contacts and noncontact force between the particle and surrounding particles or walls. The noncontact forces may originate from sources such as the liquid bridge force, van der Waals force, electrostatic force, or magnetic force (Olaleye *et al.*, 2019). In this study, the focus is on the liquid bridge force as well as the van der Waals interactions.

Each timestep, by numerically integrating the acceleration, both particles velocities and positions get updated, *i.e.*

$$x(t + \Delta t) = x(t) + v(t)\Delta t, \qquad (\mathbf{2-10})$$

$$v(t + \Delta t) = v(t) + a(t)\Delta t, \qquad (\mathbf{2-11})$$

where x(t) is the position, a(t) is the acceleration of the particle at a given time t. Both translation velocities, rotation velocities, and particle orientations are updated in this way.

As proppant transport include the fluid phase, Computational Fluid Dynamics (CFD) has been utilized for this purpose. Proppant transport in hydraulic fracturing is a multiphase flow problem. The Dense Discrete Phase Model (DDPM) has introduced into the simulation to simulate multiphase in CFD. DDPM is derived from a combination of the discrete phase model and the two-fluid model (Gidaspow, 1994)The governing equations of DDPM are discussed here briefly. The mass conservation for fluid phase and proppant particles as

$$\frac{\partial}{\partial t}(\alpha_f \rho_f) + \nabla(\alpha_f \rho_f \overrightarrow{v_f}) = 0, \qquad (\mathbf{2-12})$$

$$\frac{\partial}{\partial t}(\alpha_s \rho_s) + \nabla(\alpha_s \rho_s \overrightarrow{v_s}) = 0, \qquad (\mathbf{2-13})$$

where α_f is volume friction of the fluid, α_s is volume friction of particles, ρ_f is fluid density, ρ_s is proppant density, $\overrightarrow{v_f}$ is fluid velocity, $\overrightarrow{v_s}$ is particle velocity, and t is time. The second step is satisfying the momentum conservation for both fluid and particles, separately

$$\frac{\partial}{\partial t}(\alpha_f \rho_f) + \nabla(\alpha_f \rho_f \overrightarrow{v_f} \overrightarrow{v_f}) = -\alpha_f \nabla P + \nabla \tau_f + \alpha_f \rho_f \vec{g} + \beta(\overrightarrow{v_s} - \overrightarrow{v_f}), \qquad (\mathbf{2-14})$$

$$\frac{\partial}{\partial t}(\alpha_s \rho_s) + \nabla(\alpha_s \rho_s \overrightarrow{v_s} \overrightarrow{v_s}) = -\alpha_s \nabla P + \nabla \tau_s + \alpha_s \rho_s \vec{g} + \beta(\overrightarrow{v_s} - \overrightarrow{v_f}), \qquad (\mathbf{2-15})$$

where P is the pressure shared by all phases, τ_f is the stress tensor of the fluid phase, τ_s is the stress tensor of the solid phase, $\vec{g}$ is the gravity acceleration, β is two-phase drag coefficient which is given as following equations

$$\beta = \begin{cases} 150\dfrac{\alpha_s(1-\alpha_f)\mu_f}{\alpha_f {d_s}^3} + 1.75\dfrac{\alpha_s \rho_f |\overrightarrow{v_s} - \overrightarrow{v_f}|}{d_s}, & \alpha_s > 0.2 \\ \dfrac{3}{4} C_D \dfrac{\alpha_s \alpha_f \rho_f |\overrightarrow{v_s} - \overrightarrow{v_f}|}{d_s} {\alpha_f}^{-2.56}, & \alpha_s \le 0.2 \end{cases}, \qquad (\mathbf{2-16})$$

where d_s is proppant diameter and C_D is drag coefficient.

The fracturing fluid is essentially shear-thinning fluid to improve proppant transport *i.e.* the apparent viscosity of shear-thinning fluid would decrease as the shear stress increases. The

viscosity can be described was power law of shear deformation rate. For incompressible Newtonian fluid, a rate of deformation tensor $\bar{\bar{D}}$ can be defined as a linear function of the shear stress. The detailed equation shows below

$$\bar{\bar{\tau}} = \mu\bar{\bar{D}}, \tag{2-17}$$

where deformation rate $\bar{\bar{D}}$ is defined by

$$\bar{\bar{D}} = \left(\frac{\partial u_j}{\partial x_i} + \frac{\partial u_i}{\partial x_j}\right), \tag{2-18}$$

and μ is the viscosity which is a scalar independent of $\bar{\bar{D}}$. Similarly, for non-Newtonian fluids, the viscosity is expressed via a function η of Das following

$$\bar{\bar{\tau}} = \eta\left(\bar{\bar{D}}\right)\bar{\bar{D}}. \tag{2-19}$$

η can be a function of all three invariants of $\bar{\bar{D}}$. In this simulation, η is treated as a function of the shear rate $\dot{\gamma}$ which can be written as

$$\dot{\gamma} = \sqrt{\frac{1}{2}\bar{\bar{D}}:\bar{\bar{D}}}. \tag{2-20}$$

The power-law fluid viscosity can be defined by the following equation

$$\eta = k\dot{\gamma}^{n-1}H(T), \tag{2-21}$$

where k is a measure of the average viscosity of fluid (the consistency index), n is a measure of the deviation of the fluid from Newtonian (the power law index), the value n determines the class of the fluid. n < 1 indicates shear-thinning fluid (pseudo-plastic), n = 1 indicates Newtonian fluid, n > 1 indicates shear-thickening fluid (dilatant fluids). When temperature is considered as a constant value, H(T) is 1.

The CFD-DEM simulation is performed by a DEM software and a CFD software separately. The two software is coupled with each other to perform a coupling simulation. When performing the coupling simulation, DEM integrates fluid drug forces and torques into the particle

simulation on an individual particle level. To be more accurate, DEM first generates particles and detect contacts. Then calculate the gravitational and collision forces based on the contact models. DEM would further update the position and other parameters of particles and transfer the data to CFD simulation. Based on those data, Ansys Fluent would calculate the force performed on particles again and send it back to DEM as the new force information to initiate a new time step. The simulation cycle of the coupling simulation shows below.

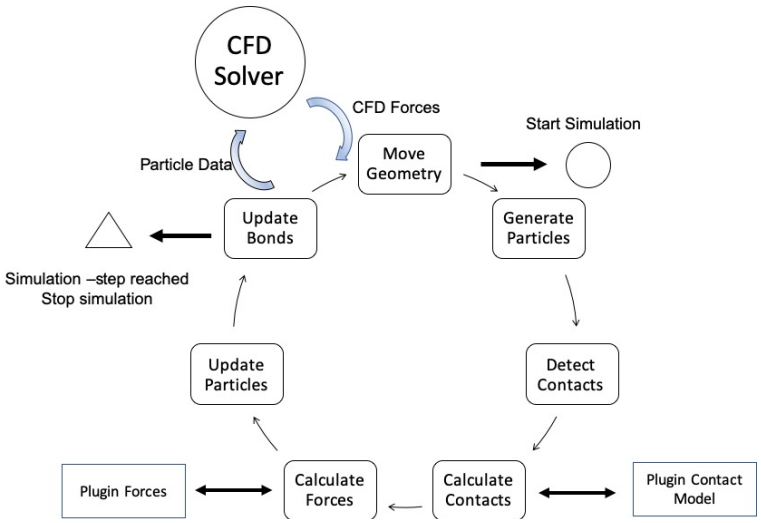

Figure **2-1**: Calculation cycle of CFD-DEM coupling model

Chapter 3

Scaling Analysis

The most accurate approach to simulate proppant transport inside the fracture is obviously tracking each individual proppant particles to avoid miscalculations or errors involved in simplifying problem by assigning continuous concentration of particles which neglects particles interactions such as clamping or collision or friction between particles. In this approach one may show proppant settlement and erosion under one frame but such a detailed model in the form of a coupled CDF-DEM would require extensive computational resources to accommodate modelling of individual particles and their interactions. In a typical hydraulic fracturing job in the field billions of these particles may be used but we do not necessarily need to model such a huge problem to understand the mechanisms behind proppant placement during hydraulic fractures as these deterministic models may need month to be run on parallel supercomputers to deliver a solution which would be limited to a very specific geometry. One solution to address this computational burden is scaling down the problem to the dimension sizes that can be better handled with the available computational power. This approach would be similar to what has been traditionally done in fluid dynamic experiments. By a correct scaling, one should expect to observe similar phenomena at a much smaller scale. A small model would enhance the efficiency of the simulation and reduce the calculation time. The main purpose of our scaling analysis is to recognize important dimensionless parameters involved in the proppant transport by verification through numerical experiments. By keeping the value of the dimensionless parameters constant, the impact of the scale of the model can be compensated.

Proppant transport is a complex process that involves various physical and chemical interactions between solid and liquid phases. To better understand the whole process and perform a proper scaling analysis on the proppant transport, key parameters which mentioned above should

be identified first. The parameters involved in the proppant transport include rheology of the fluid (μ), fluid velocity ($\overrightarrow{v_f}$), density of fluid (ρ_f), concentration of proppants (C_s), density of proppant (ρ_s), proppant velocity ($\overrightarrow{v_s}$), diameter of proppant(d_s), proppant shape (roundness and sphericity), fracture height (H), fracture length (L), fracture width (e) and fracture shape. Considering many parameters influence this problem, using the governing equations as well as the characteristic forces that applied on both particle and fluid, we performed a scaling analysis.

The scaling analysis is based on two fundamental principles. One is to keep the similarity of the geometry and the other is to keep the relations between different parameters during the analyze process. The concept of fixing a problem's geometry and considering only changes to the absolute length scale of the shape is called geometric similarity (Santiago, 2019). The importance of keeping geometry similarity is to keep the factors related to the shape being constant, as the scale of the geometry do change within the analysis. When applying this principle into proppant transport problem, the major concern is how to change the fracture shape in the absolute length scale. Thus, to ensure geometric similarity, the following dimensionless number can be used

$$D_1 = \frac{H}{L}, \qquad (\mathbf{3-1})$$

where H is the height of the fracture and L is the length of the fracture. D_1 is height to length ratio of fracture.

Governing equations are crucial to keeping the relations between different parameters during the analysis process. This is not meaning that we need to keep the actual relation between each parameter. We only need to focus on the key parameters that must be involved in the analysis process. The governing equations govern the relations between different parameters. As the simulation of proppant transport is composed of both fluid flow and particle motion, the derivation of any dimensionless number must consider the governing equation for each component.

The analysis is performed using Ipsen's method. The Ipsen's method is first introduced by David Carl Ipsen. The purposed of this method is to derive a functional relationship in terms of nondimensional groups of parameters. The procedure (Santiago, 2019) can be described as following. First, the key parameters should be identified as well as the dimensions of those parameters. Then, based on the governing equations, hypothesize some functions of interest. Next, a parameter that contain the primary dimension that need to be eliminated should be clarified. Last, by multiple or dividing selected parameter to eliminate the remaining parameters that contains the primary dimension selected. Following the steps above, dimensional analysis below can be performed.

From momentum conservation for fluid and particle as shown in Eqs.2-14 to 2-16, the key parameters can be defined as: $\alpha_s,\ \alpha_f, \tau_f, \rho_s, \rho_f,\ g,\ v_s,\ v_f,\ d_s,\ \mu,\ t.$ Then the function of interest can be written as

$$P = f\left(\alpha_s,\ \alpha_f, \tau_f, \rho_s, \rho_f,\ g,\ v_s,\ v_f,\ d_s,\ \mu,\ t\right). \qquad (3-2)$$

Then the following dimensionless parameters can be obtained

$$D_2 = \frac{\alpha_s}{{d_s}^3} \qquad D_3 = \frac{\alpha_f}{{d_f}^3} \qquad D_4 = \frac{\tau_f}{\rho_s\ {v_s}^2} \qquad D_5 = \frac{g d_s}{{v_s}^2} \qquad (3-3)$$

$$D_6 = \frac{v_f}{v_s} \qquad D_7 = \frac{\mu}{\rho_s d_s v_s} \qquad D_8 = \frac{v_s}{t d_s}$$

From drag force and particle interaction force, using the same approach, the following new parameters can be obtained. The drag force can be written as

$$\overrightarrow{F_d} = D_p\left(\overrightarrow{v_f} - \overrightarrow{v_s}\right) m, \qquad (3-4)$$

$$D_p = \frac{3}{8S_g} C_d \frac{2\left|\overrightarrow{v_f} - \overrightarrow{v_s}\right|}{d_s} . \quad (3-5)$$

S_g is the specific gravity, m is the mass of particles and C_d is drag coefficient which related to A, fracture surface area.

Then the following dimensionless parameters can be obtained

$$D_9 = \frac{\rho_s {d_s}^3}{m} \quad D_{10} = \frac{\mu {d_s}^2}{v_s m} \quad D_{11} = \frac{A}{{d_s}^2} \quad (3-6)$$

When considering the friction among the particles, new parameters could be identified from eq. 3-7.

$$F_f = -\alpha_s \nabla P + F_d . \quad (3-7)$$

The following dimensionless parameter can be obtained

$$D_{12} = \frac{P}{\rho_s {v_s}^2} \quad (3-8)$$

Although there are twelve dimensionless parameters that have been directly derived from the governing equations of this problem, the significance of each one of these parameters still need to be investigated to select the ones that should be considered for scaling purposes.

During the past decades, several dimensionless parameters have been introduced into the study of fluid mechanism as well as the multiphase flow. For example Stokes number is used to characterize the behavior of particles suspended in a fluid flow, whereas Froude number represents the inertial force divided by gravitational force. The ratio of Stokes number to Froude number can present the interaction among phases and ensure the same transport conditions of particles in different scales.

In order to ensure the accuracy of scaling analysis, the dimensionless variables used in this paper are picked from previous studies. The above twelve dimensionless parameters would filter the existing dimensionless parameters from previous studies. All the chosen parameters could be derived by applying the basic algorithm on the above twelve dimensionless parameters. Based on

this selection criterion, the following dimensionless variables have picked: Stokes number to Froude number ratio, Shield number, Reynolds number, Buoyancy number, proppant density to fluid density ratio, and fracture height to length ratio. Each one will be discussed briefly in followings.

As proppant transport is a multiphase flow, both fluid phase and solid phase would involve in the numerical model. When reduce the scale of the fracture geometry model, the interaction among phases would also be impacted. Thus, to compensate such impact, Stokes number, St, to Froude number, Fr, ratio has been introduced to this study (Shrivastava and Sharma, 2018)

$$\frac{S_t}{F_r^2} = \frac{mg}{6\pi d\mu} \,. \qquad (3-9)$$

Shield number has also picked to reduce the impact of scaling down (Jordan, 2013; Patankar *et al*., 2002). Shield number is the ratio of the shear force to the gravitational force on a particle of sediment. This number is widely used to quantify the bed load transport behavior which is driven by erosion forces. Shield number could be obtained as $\frac{D_4}{D_5}$.Based on the definition, Shield number is

$$\theta = \frac{\mu v}{(\rho_s - \rho_f) \times g \times d \times e}, \qquad (3-10)$$

where d is the diameter of particle and e is the fracture width. Another parameter selected for reducing the scale of the model is Reynolds number. The Reynolds number is the ratio of inertial forces to viscous forces within a fluid, and it is subjected to relative internal movement due to different fluid velocities. Reynolds number is majorly used to predict flow patterns in different flow situations. By keeping a constant Reynolds number, the flow pattern in different scales can be then locked. Reynolds number has been derived from governing equations as $1/D_7$. In this study, both Reynolds number of fracture and Reynolds number of particles have been applied. The Reynolds number for a fracture model which formed by parallel plates can be express as

$$Re_{frac} = \frac{\rho v 2e}{\mu}\ , \qquad (3-11)$$

where ρ is fluid density, v is fluid velocity, e is fracture width, μ is the viscosity of fluid.

The Reynolds number of particles can be written as

$$Re_{prop} = \frac{\rho v d}{\mu}, \qquad (3-12)$$

where ρ is fluid density, v is fluid velocity, d is the diameter of particle, μ is the viscosity of fluid.

To represent the competition between gravity and buoyancy, Buoyancy Number (Fernández *et al.*, 2019; Patankar *et al.*, 2002) could be a good representative,

$$B_u = \frac{\rho g e^2}{\mu v}\ . \qquad (3-13)$$

By comparing this equation with the dimensionless parameters derived above, Buoyancy number is basically the ratio of D_5 to D_7. This dimensionless number is introduced in the paper of Fernández *et al.*(2019) regarding proppant transport in a scaled vertical planar fracture.

Gravity is another crucial force playing in the proppant transport. When considering the impact of gravity, the following dimensionless parameter has been introduced as

$$\frac{\rho_{prop}}{\rho_{fluid}}, \qquad (3-14)$$

where ρ_{prop} is the density of proppant and ρ_{fluid} is the density of fluid.

Besides the above-mentioned dimensionless variables, in order to ensure geometric similarity, the fracture height to length ratio should be also included in the analysis. Therefore, we ended up with there are six dimensionless variables has been selected.

Chapter 4

Results and Discussions

Using the above dimensionless variables, several simulation cases were performed to study proppant transport in scaled hydraulic fracture systems. Case *1* is the basic case i.e., a planar fracture which provides a benchmark for comparison with other studies. Case *2* extends the fracture geometry to a scaled T-shaped fracture. Case *3* introduces the precision of scaling analysis. A comparison between the results of lab experiments and numerical simulation is also provided. Case *4* involves a bypass fracture to determine the impact of fracture intersections on proppant distribution in fracture networks. Case *5* looks at the role of proppant concentration on proppant displacement. Case *6* provides a sensitivity study for different proppant sizes. Finally, case *7* uses different injection rates to understand the effect on the final distribution of proppants.

Case 1: Planar Fracture Case

By using the dimensionless variables obtained from the scaling analysis, a planar fracture model has been constructed. *Figure 4-1* shows the computational geometry and mesh. Several parameters were introduced into the study to ensure the quality of the mesh e.g., resolution, which is used to control the mesh distribution; a higher resolution value refers to a finer mesh. The parameters can be determined as follows. Within the meshing process, the resolution is *7*, the bounding box diagonal is *0.23717 m*, the average surface area of the geometry model is *0.01044* m^2, the minimum edge length in the geometry is *0.008 m*. To retain the high quality of the mesh, three parameters are defined within the mesh quality control process. The first is the target skewness, which determines how close to ideal triangles or quadrilaterals a face or cell is. The

second is the transition ratio, which controls the growth of the adjacent elements around the boundaries. The third is the growth rate, which determines the relative thickness of adjacent inflation layers. In this case, the target skewness is limited to *0.9* to maintain an acceptable cell quality, the transition ratio is *0.272* based on the physics preferences of the CFD model, and the growth rate is *1.2* which would result in a *20*% increase in the edge length of elements. *Figure 4-1* introduces a vertical planar fracture geometry model. The inlet of the fracture is marked in blue, with a slot added to represent the fracture. The elements in gray represent the slot-shaped fracture. Inside the fracture is the fracturing fluid, which is in the middle of the model. Proppant slurry is injected through the inlet and flows out of the fracture via the outlet. The details of the dimensions and dimensionless parameter values are listed in *Table 4-1*.

Table **4-1**: Fracture dimensions and properties

Property	**Filed**		**Simulation**	
Fracture Height	40	m	0.1	m
Fracture Length	80	m	0.2	m
Fracture Width	8	mm	8	mm
Fluid Injection Velocity	0.33	m/s	0.33	m/s
Proppant Injection Velocity	0.33	m/s	0.33	m/s
Poisson's Ratio	0.25	Pa	0.25	Pa
Shear Modulus	1e+10	Pa	1e+10	Pa
Fluid Density	1000	kg m^{-3}	1000	kg m^{-3}
Solids Density	2533	kg m^{-3}	2533	kg m^{-3}
Fluid Viscosity	0.001	kg m^{-1} s^{-1}	0.001	kg m^{-1} s^{-1}
Re Fracture	5.3e+7		5.3e+7	
Re Fluid	3300		3300	
Buoyancy Number	1900		1900	
Shield number	0.69		0.69	
Fluid Solid Density Ratio	2.533		2.533	
Stokes to Froude Ratio	0.4865		0.4865	
Fracture Height to Length Ratio	0.5		0.00272	

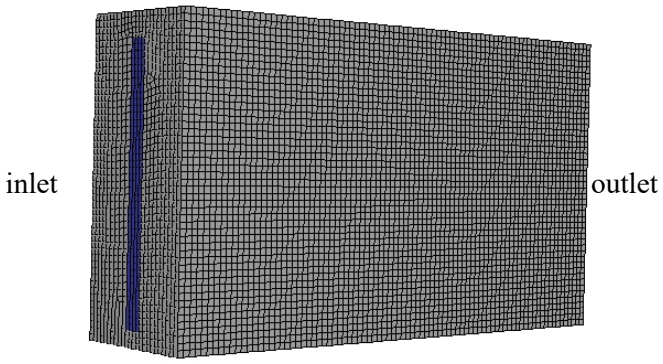

Figure **4-1**: The geometry of the model and mesh of Case *1*

The particles are generated in the DEM simulation at the fixed rate of *33567* particles per second and are allocated random positions at the inlet cross-section. This particle rate corresponds to the proppant load of about *0.4 lb./gal.* Detailed properties of these particles are listed in *Table 4-2*. The initial velocity of each particle equals the fluid velocity of *0.33 m/s* at the inlet, which is the injection velocity at the fracture mouth. To describe the shear-thinning behavior of the fluid, the consistency index is defined as *0.0122* Kgs^{n-2}/m, the power-law index is *0.727*, the minimum viscosity limit is *0.001 kg/ms*, and the maximum viscosity limit is *0.6 kg/ms*. The boundary conditions for CFD simulations have been defined so that at the inlet, the velocity is constant at *0.33 m/s*. For the outlets, the pressure is assumed to be equal to the reservoir pressure, or zero net pressure.

Table **4-2**: Particle Properties

Parameter	Value	Unit
Particle size	30/70	mesh
Poisson's Ratio	0.25	----
Solids Density	2660	Kg/m^3
Shear Modulus	1e +7	Pa
Young's Modulus	2.5e +7	Pa
Coefficient of Restitution	0.5	----
Coefficient of Static Friction	0.1	----
Coefficient of Rolling Friction	0.01	----

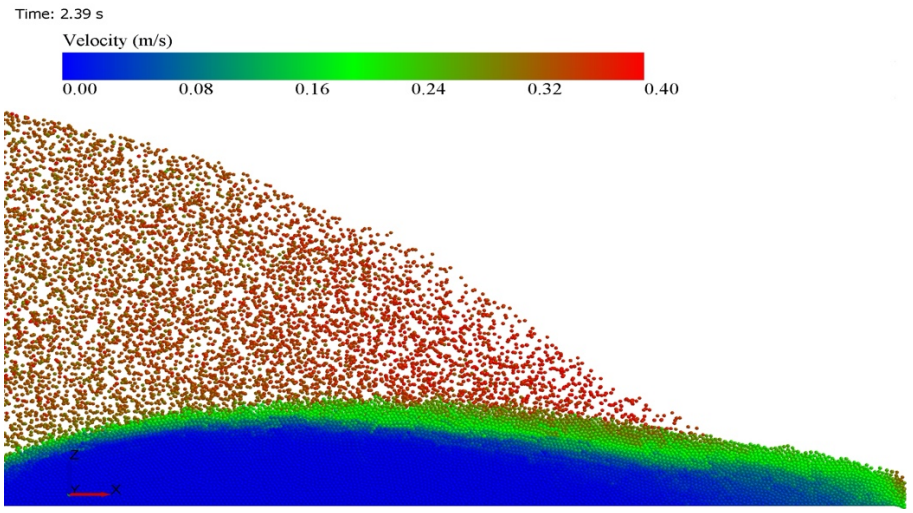

Figure **4-2**: Proppant distribution at an earlier stage of Case *1*

Initially, there were no proppants inside the fracture. *Figure 4-2* shows the proppant distribution early after starting the injection. After injecting *3.3* primary fracture volumes of proppant slurry, the proppants settled at the bottom of the fracture. When considering the proppant deposition and displacement behavior, the results obtained from the simulation are consistent with the results reported by Kera *et al.* (1956). The zones identified by Kera *et al.* (1956) can be observed throughout these simulation results. The sands injected earlier deposit near the inlet, whereas the proppant injected later keeps moving deeper into the fracture. The deposited sands form an immobile sand zone and a mobile sand zone. A slurry zone could be observed ahead of this zone as well. Around the outlet, a clear fluid zone could also be identified. *Figure 4-3* (a) shows our simulation results after injecting *1.65* primary fracture volumes of proppant slurry. *Figure 4-3* (b) is a schematic figure of sand transport in a vertical planar fracture, adapted from the lab observations of Kera *et al.* (1956).

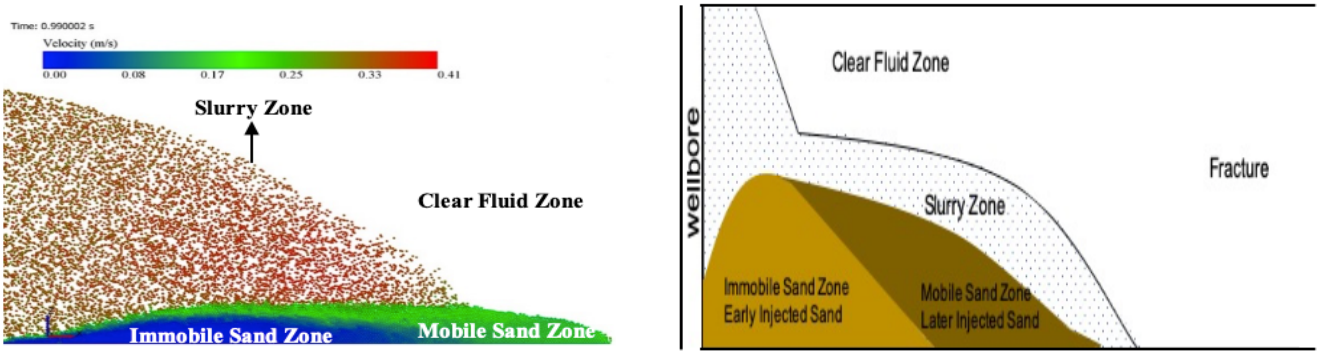

(a) **(b)**

Figure 4-3: Comparison of proppant deposition and transport between simulation result and lab experiment results by Kera et al. (1956)

Figure 4-4 shows the final distribution of proppants. The proppant particles tend to deposit primarily near the inlet of the fracture. The maximum height of the sand dune is located close to the fracture inlet, with the maximum equilibrium height of the sand dune reaching *67 mm*, which is *67*% of the fracture height. Based on the motion of the injected proppants, three zones can be identified: slurry flow zone, surface rolling zone, and sand bed zone. As seen in *Figure 4-4*, proppants are sorted by their velocity. Particles with a lower velocity are marked in blue, and particles with a higher velocity are marked in red. Particles in the slurry flow zone are transported by the fluid and usually have a higher velocity, and the drag force from the fracturing fluid is the dominant force on particles in this zone. In contrast, particles in the sand bed zone are static as the primary force in this zone is the friction between particles and fracture surface. In the transition from slurry flow zone to sand bed zone, the surface rolling zone usually has a moderate velocity. The particles in this zone move through the surface of the deposited sand bed and some particles in this zone also settle in the sand bed zone. The dominant force in the surface rolling zone is the friction between the particles.

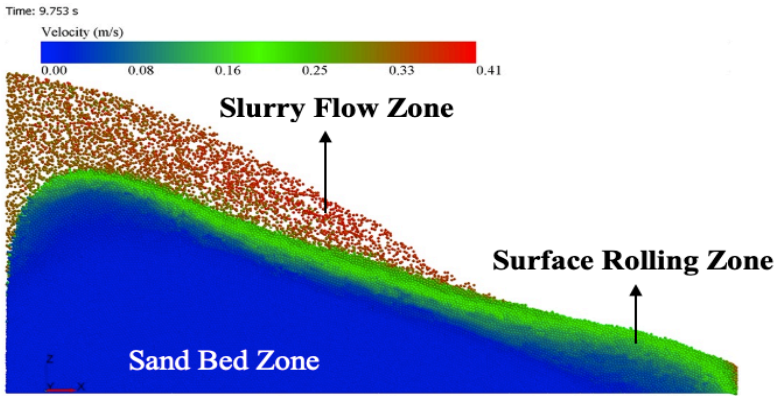

Figure **4-4**: Final distribution of proppants in Case *1*

Fernández *et al.* (2019) performed an experiment in a scaled single fracture in which *30/70* mesh sized proppants are injected at a rate of *0.33 m/s*. The concentration of the proppant slurry equals *0.4 lb./gal* and the length to height ratio of the primary fracture is *0.5*. *Figure 4-5* shows a comparison between our simulation results *(a)* and the Fernández *et al.* (2019) lab experiment *(b)* in terms of proppant distribution. In both simulation results and lab experiment results, the proppants start to deposit around the inlet, and the maximum height of the sand dune remains around the inlet of the fracture; however, in the experiment the maximum height of the sand dune moves further into the fracture. Moreover, since the slot used in the lab experiment is a closed-end slot, a high concentration of proppant particles can be identified at the end of the fracture.

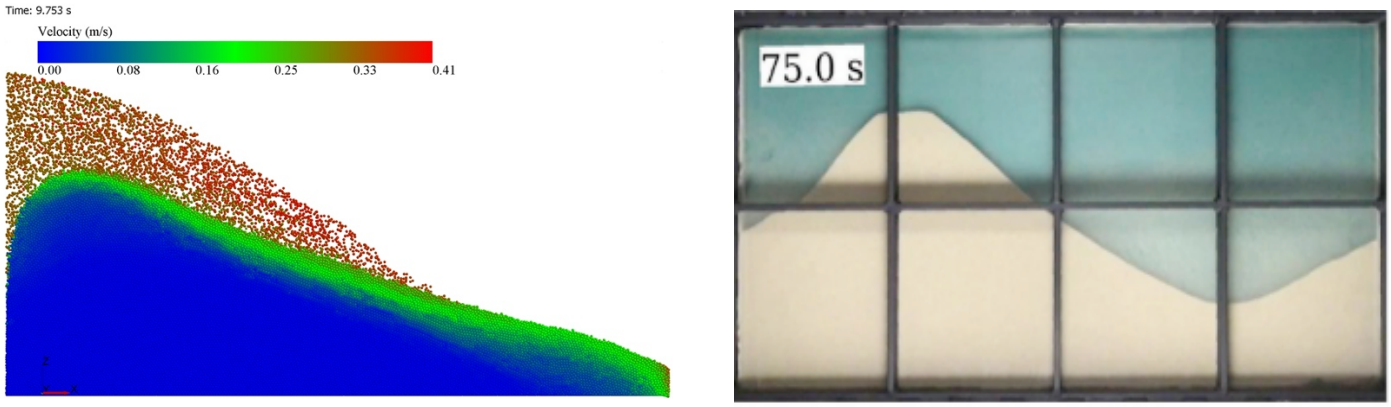

(a) **(b)**

Figure **4-5**: Comparison of simulation result and lab experiment result of Case *1*

The simulation involves both the solid and fluid phase, and *Figure 4-6* shows the flow velocity vector of the fracturing fluid. Lines in the figure indicate the flow path of the fluid, and the color indicates the velocity. *Figure 4-6* shows that the sand dune formed previously would impede the injection of proppant slurry, and a partial high-velocity zone is identified around the inlet. *Figure 4-7* shows the maximum pressure difference between inlet and outlet. As shown in the figure, at the beginning of the simulation only a few proppants are involved in the simulation, and thus a lower pressure difference is required to transport them. Then, as the proppants start to deposit and the sand dune starts to develop, a higher pressure difference is required to maintain the transportation at the initial rate but in limited fracture cross-section. As the sand dune reaches equilibrium height, the pressure difference trends to a constant value.

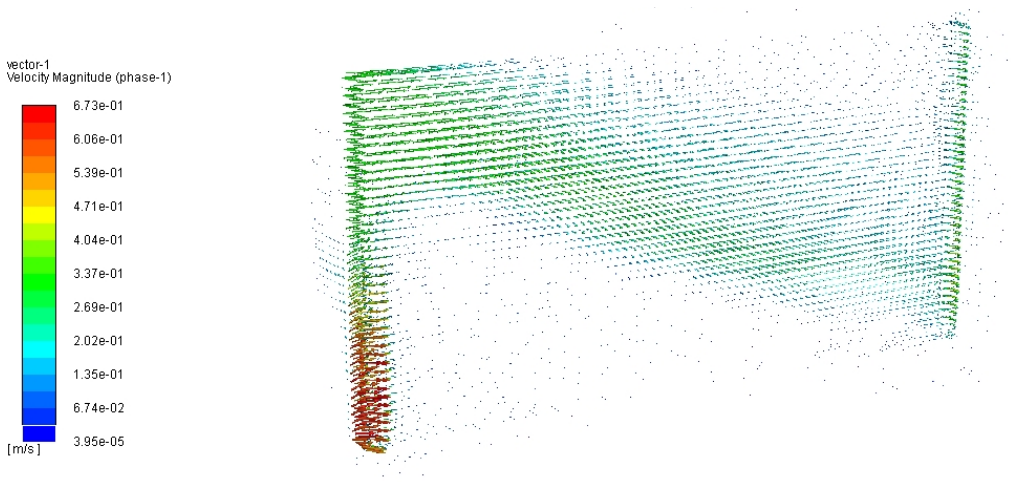

Figure **4-6**: Interaction between fluid and particles in Case *1*

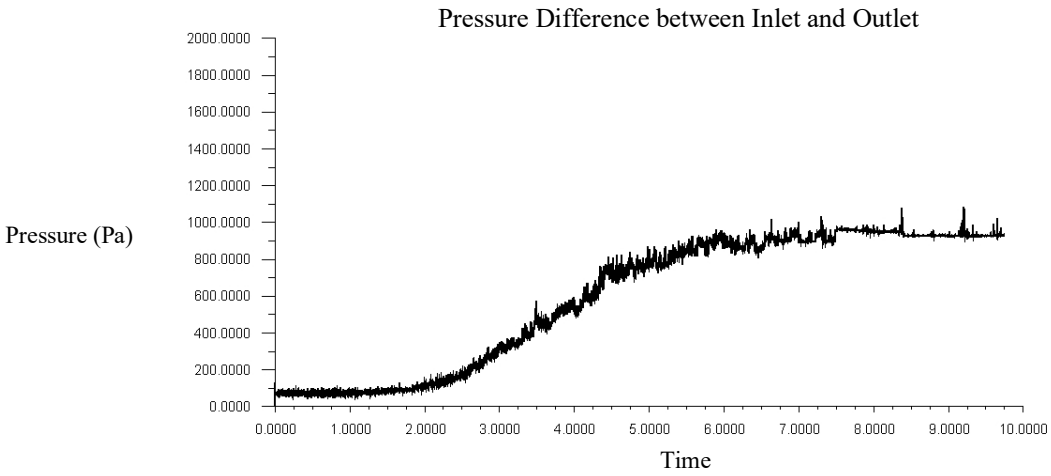

Figure **4-7**: Pressure difference between inlet and outlet in Case *1*

Case 2: T-Shaped Fracture Case

Case *2* represents a T-shaped fracture. *Figure 4-8* shows the computational geometry and mesh. The inlet of the fracture is marked in blue with the two outlets marked in red. A slot has been constructed to represent the fracture. The elements in gray represent the wall of the slot-shaped fracture. Inside the fracture is filled with the fracturing fluid. The meshing strategy in Case *2* is the same as Case *1,* and the parameters required for the meshing process are as follows: the resolution is *7*, the bounding box diagonal is *2.3439 m*, the average surface area is *0.222294* m^2, the minimum edge length is *0.006 m*, the target skewness is limited to *0.9*, the transition ratio is *0.272,* and the growth rate is *1.2*. As the injection velocity, fracture dimensions, fluid rheology and proppant properties are the same as Case *1*, the values of dimensionless variables in Case *2* did not change. The details of the dimension of the geometry and some values of the critical dimensionless parameters are listed in *Table 4-3*.

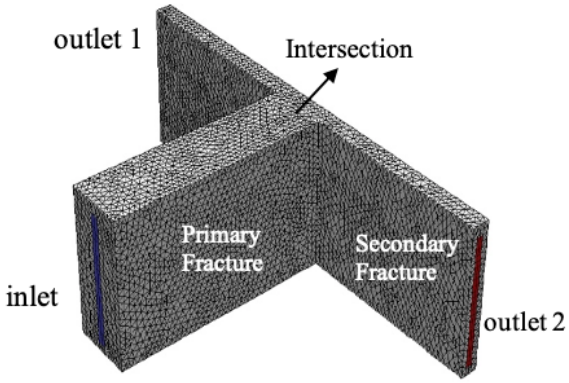

Figure **4-8**: The geometry of the model and mesh of Case *2*

Table **4-3**: List of dimensions for the filed reference fracture and the simulation model of Case *2*

Property	**Filed**		**Simulation**	
Fracture Height	40	m	0.1	m
Fracture Length (Half Wing)	80	m	0.2	m
Fracture Width	8	mm	8	mm
Fluid Injection Velocity	0.33	m/s	0.33	m/s
Proppant Injection Velocity	0.33	m/s	0.33	m/s
Fracture Height to Length Ratio	0.5		0.5	

The particles are generated in the DEM simulation at the fixed rate of *33567* particles per second and are allocated random positions at the inlet cross-section. The load of the proppant slurry is assumed to be *0.4 lb./gal*. The initial velocity of each particle is *0.33 m/s*. The physical parameters of the model are the same as Case *1*. The boundary conditions for CFD simulations are defined as the velocity is kept constant at *0.33 m/s* at the inlet. As for the two outlets, the pressure remains equal to the reservoir pressure *i.e.*, zero net pressure.

Figure 4-9(a) shows early proppant distribution in the primary fracture. After injecting *8.93* primary fracture volumes of proppant slurry, much of the proppant dune is developed and keeps growing while the proppants are transported into the secondary fracture. *Figure 4-9 (b)* shows proppant distribution in the secondary fracture after injecting *8.93* primary fracture volumes of proppant slurry. Proppants start to settle at the intersection (the end of the primary

fracture), and the maximum height of the sand dune reaches equilibrium in this position. The proppant dune keeps growing, and a uniform sand bed growth rate can be observed over the whole fracture network. *Figure 4-10 (a)* shows proppant distribution in the primary fracture at later stages. After injecting *33* primary fracture volumes of proppant slurry, as more proppants settle, the sand dune becomes steeper. The slope of the sand dune is decided by the angle of repose, which is related to the proppant material. *Figure 4-10 (b)* shows proppant distribution in the secondary fracture after injecting *33* primary fracture volumes of proppant slurry. As the proppants are transported further, the maximum height of the proppant dune is located in the middle of the fracture. The distribution of proppant can be observed as symmetric in the two half-wings.

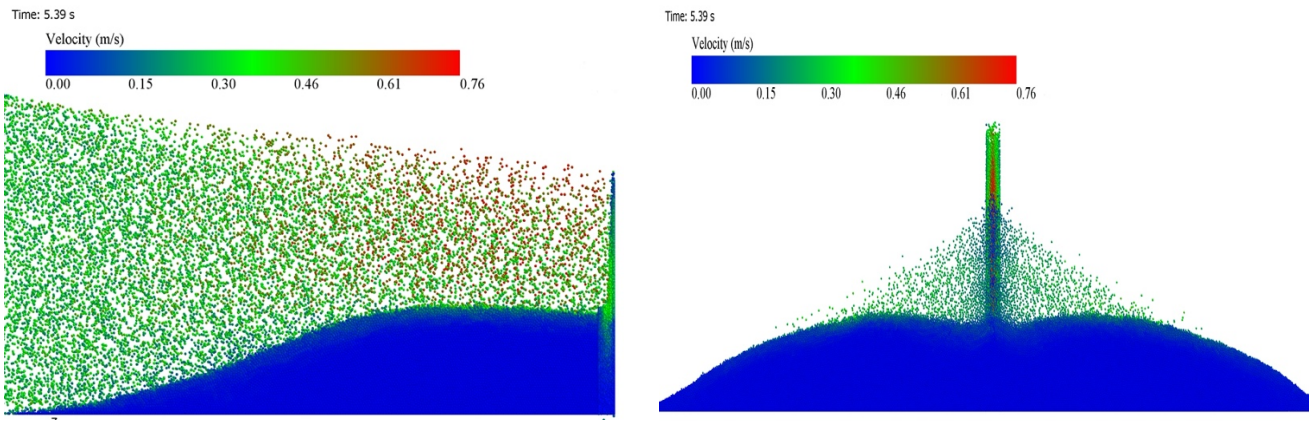

(a) **(b)**

Figure **4-9**: Proppant distribution of Case *2* after injecting *8.93* primary fracture volumes of proppant slurry

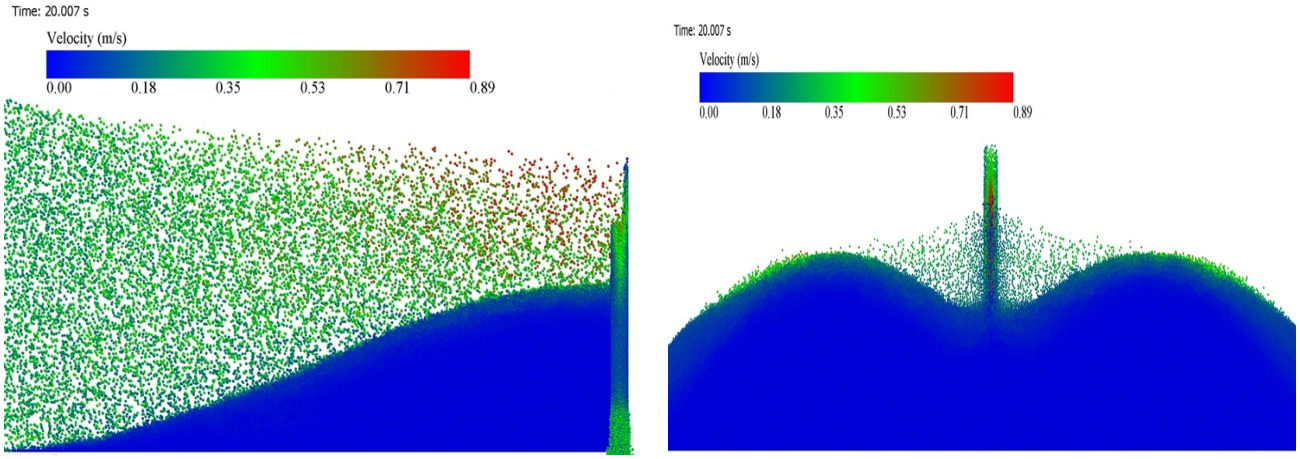

(a) **(b)**

Figure **4-10**: Proppant distribution of Case *2* after injecting *33* primary fracture volumes of proppant slurry

When compared to the results of Case *1*, in the presence of a secondary fracture, the sand dune in the primary fracture shifts toward the intersection of the fracture network, the equilibrium height of the sand dune is reduced, and the location of the maximum height of the dune moves from the inlet to the intersection.

Figure 4-11 shows the final distribution of proppants in the fracture network. The height of the sand dune formed in the primary and secondary fractures has reached equilibrium height. The sand dune's maximum equilibrium height in the primary fracture is *43 mm*, which is *43*% of the designed fracture height, and its maximum equilibrium height in the secondary fracture is *62 mm*, which is *62*% of the designed fracture height. The final distribution shows that the equilibrium height in the secondary fracture could be higher than the primary fracture, however, this observation is largely dependents on the distance of the intersection point from the injection well. Obviously if the intersection point is long enough from the injection well, very few proppants may reach to the secondary fracture. In addition to the parameters that govern sand dune formation in planar fractures, fluid velocity changes at the fracture intersection points could be a critical factor in settlement of proppant particles and forming these sand dunes as seen in this example. *Figure 4-*

12 shows the proppant slurry flow zone in the fracture network for Case *2*. The slurry flow zone in Case *2* has a larger area than in Case *1* and the surface rolling zone is not as apparent as in Case *1*.

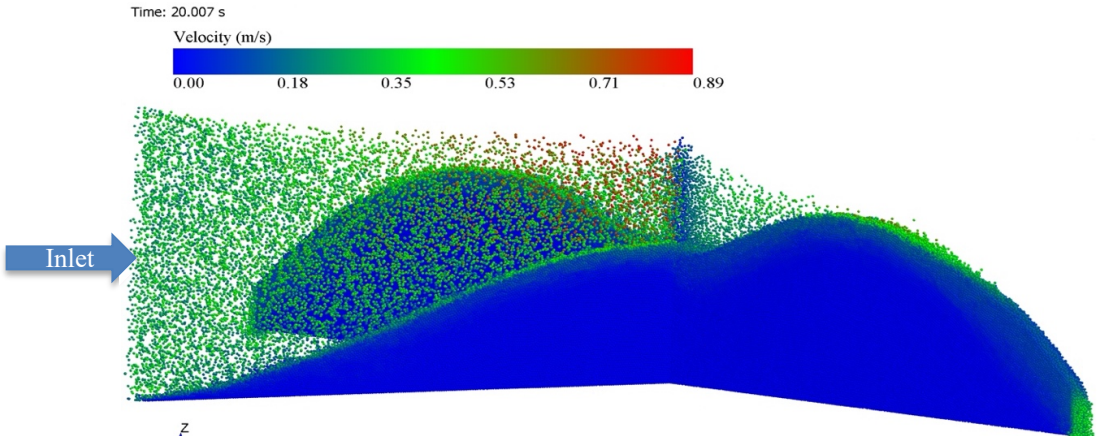

Figure **4-11**: Proppant distribution in fracture network of Case *2*

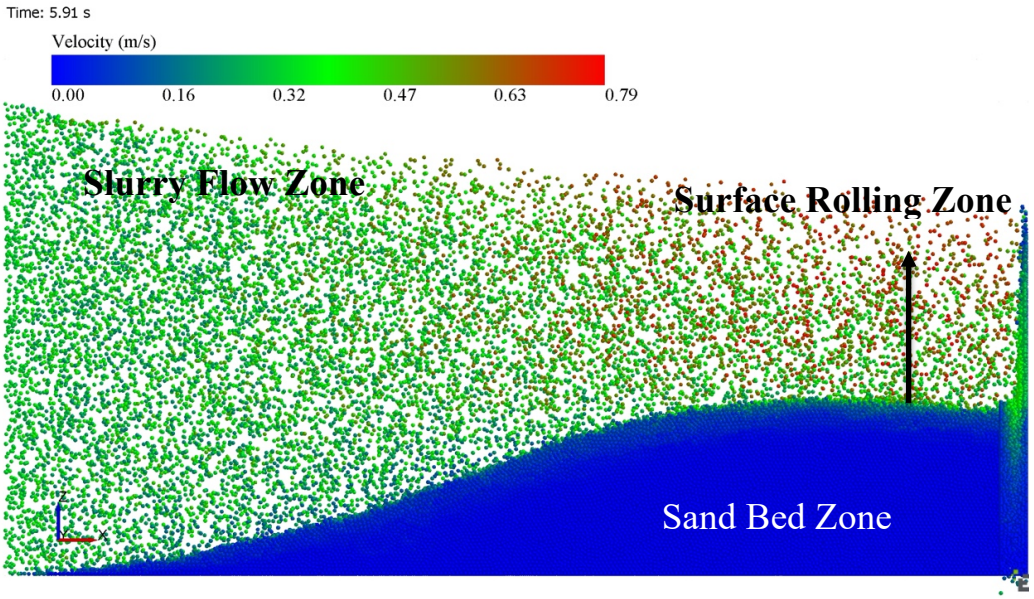

Figure **4-12**: Proppant flow zone in primary fracture of Case *2*

The proppant dune in the primary fracture reaches an equilibrium height at *7.5 s*, after injecting *12.375* primary fracture volumes of proppant slurry. The proppant dune in the secondary fracture reaches an equilibrium height at *15 s*, after injecting *24.75* primary fracture volumes of proppant slurry. The scale of time T is equal to L/V, since the scale of length L has been reduced

400 times, the scale of time would reduce *400* times as well. The operation time of *7.5 s* in the simulation would equal an operation time of *50* min on the field scale, and the operation time of *15 s* in the simulation would equal an operation time of *100* min on the field scale.

Figure 4-13 shows the number of proppants inside the fracture system during the simulation time. The solid lines in the figure indicate the slope change, which further represents the equilibrium of the proppant dunes. The slope in this plot refers to the increased number of proppants within the system. The significant change in the slope indicates that the proppant dune reached equilibrium in both the primary and secondary fractures. Moreover, the further number of proppants tends to leave the computational model without settlement.

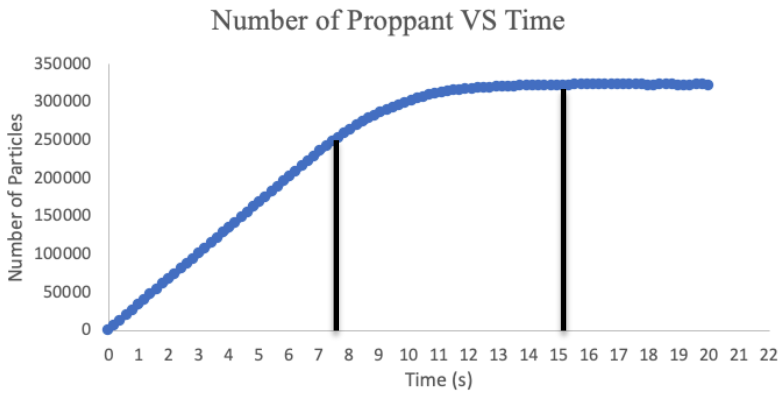

Figure **4-13**: Number of proppants in fracture during the simulation in Case *2*

The outcome of the flow in the two outlets is almost the same and these slight differences can be disregarded. The flow rate decreased as the proppant dune began to form. The flow rate continued to decrease until the proppant dune in the secondary fracture reached equilibrium. This occurred because the proppant dune formed in the fractures can affect the flow of the fracturing fluid. The severity of such an effect depends mainly on the height of the proppant dune. In addition, a significant decrease in the outflow rate occurred when the proppant dune in the primary fracture reached equilibrium.

As the simulation involved both the solid phase and fluid phase, *Figure 4-14* shows the flow velocity vector of fracturing fluid, which in turn shows the interaction between the fluid and proppant particles. Lines in the figure indicate the flow path of the fluid, and the color indicates the velocity. *Figure 4-14* shows a high-velocity zone above the surface of the sand dune. Much of the high-velocity zone is located in the slurry flow zone. Moreover, the velocity of the fluid is related to the height of the proppant bed. A higher proppant height may result in a higher fluid velocity.

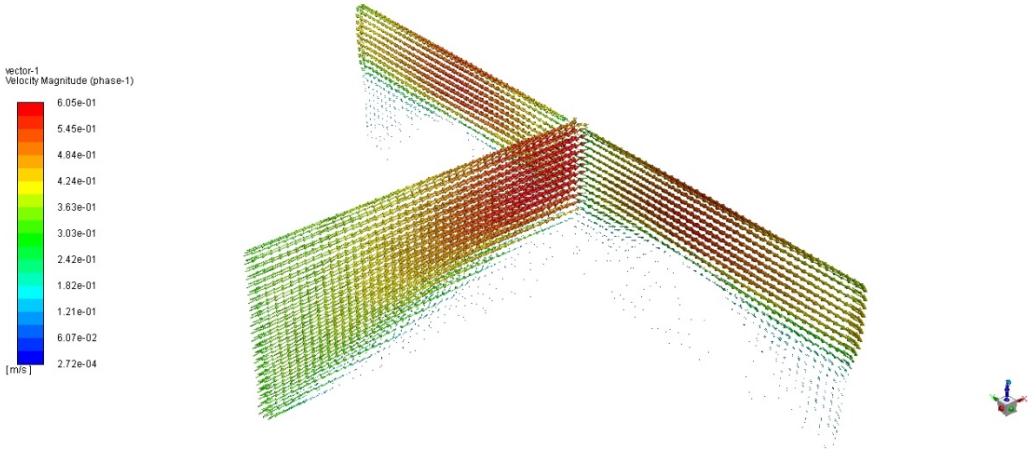

Figure **4-14**: Interaction between fluid and particles in Case *2*

As indicated earlier, the proppant distribution in a T-shaped fracture largely depends on the distance of the intersection point from the injection well. In practical cases, this distance is expected to determine by average spacing and direction of natural fractures (Dahi Taleghani *et al.*, 2018; Puyang *et al*., 2018). To further study the impact of proximity to the intersection point, the following simulations have introduced into Case *2*. By increasing the distance of the intersection point from the injection well to *1.5* times of the initial length, proppants distribution in the primary fracture further develops as shown in *Figure 12*. After injecting *10.44* times of the primary fracture volume, the proppants in the primary fracture tends to mainly deposit in the middle of the fracture (*Figure 4-15 (a)*). The sand dune then keeps moving deeper into the intersection point. *Figure 4-15 (b)* shows the final proppant distribution in the primary fracture. After injecting *47.67* times of

the primary fracture volume, most proppants have deposited around the intersection point. However, the proppant distribution in the secondary fracture remains the same as the benchmark simulation with the original distance. The sand dune's maximum equilibrium height in the primary fracture is *57 mm*, which is *57%* of the fracture height, and its maximum equilibrium height in the secondary fracture is *62 mm*, which is *62%* of the designed fracture height. When comparing this result with the simulation with the original distance, the maximum equilibrium height in primary fracture has increased significantly, but still shorter than the one in the primary fracture.

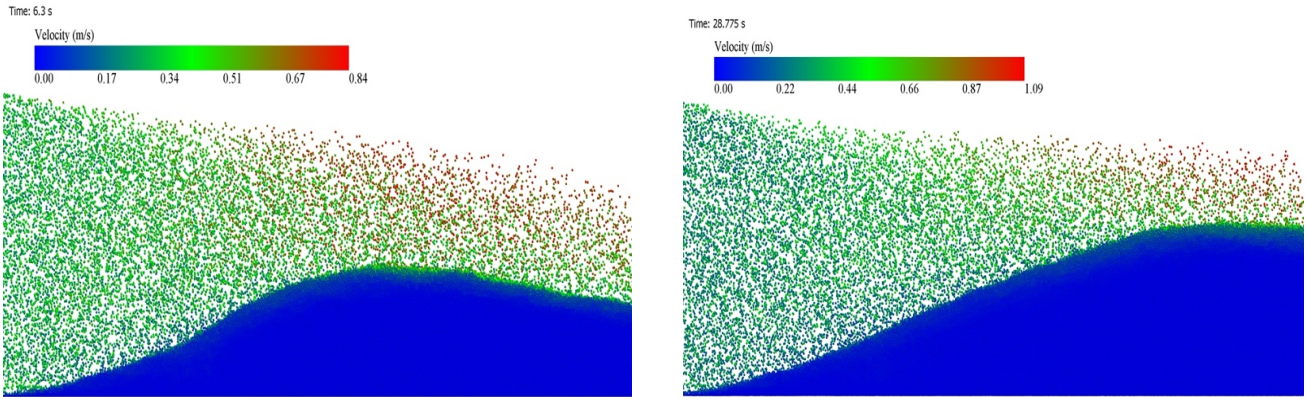

(a) **(b)**

Figure **4-15**: Proppant distribution in the primary fracture of Case *2* with 1.5 times longer distance of the intersection point from injection well

The impact of the distance of the intersection point from the injection point would be mainly on the primary fracture by increasing the maximum equilibrium height significantly. With a longer distance of the intersection point from the injection well, the proppants travel a relatively longer distance before depositing inside the fracture, then the impact of gravity gets amplified. When considering the proppants' movement mechanisms inside fractures, the deposition of proppants is caused by either gravitational force or change of the fluid momentum doe the change in the flow direction. Then an amplified impact of gravitational force would accelerate the deposition process of the proppants, which is amplified by the impact of the change of flow

direction at the intersection point. The deposited sand dune then transported further into the intersection point by the fluid. Due to the low-velocity zone located around the intersection point, most of the sand dune remains in the intersection while only a small part moves into the secondary fracture. The overall proppant distribution is the same as the previous results. When considering the final proppant distribution in the secondary fracture, the impact of distance of the intersection point from the injection well has not been identified.

Case 3: Verification of Scaling Strategy

In this study, a scaled fracture model was introduced into the numerical simulation. The accuracy and viability of this model still need to be verified, and to achieve this goal the result obtained from a larger model should be consistent with the results obtained from a smaller model, as the two models share the same dimensionless variables. Thus, a case with a fracture model on a smaller scale was performed to complete the verification process. Within the model, the dimension of the geometry model was reduced, and the value of the dimensionless variables was reserved. *Table 4-4* shows the differences in the dimensions of Case *2* and Case *3*.

Table **4-4**: Comparison of dimensions among Case *2* and Case *3*

Property	**Case 2**		**Case 3**	
Fracture Height	0.1	m	0.05	m
Fracture Length (Half Wing)	0.2	m	0.1	m
Fracture Width	8	mm	8	mm
Fluid Injection Velocity	0.33	m/s	0.33	m/s
Proppant Injection Velocity	0.33	m/s	0.33	m/s
Fracture Height to Length Ratio	0.5		0. 5	

The meshing strategy for this case is the same as Case *2*, and the detailed parameters in the mesh process are as follows: the resolution is *7*, the bounding box diagonal is *0.24013 m*, the average surface area is *0.0046919* m^2, the minimum edge length is *0.006 m*, the target skewness is

limited as *0.9*, the transition ratio is *0.272,* and the growth rate is *1.2*. The particles are generated by the DEM simulation at the fixed rate of *16783* particles per second and are allocated random positions at the inlet cross-section. The load of the proppant slurry is assumed to be *0.4 lb./gal.* The physical parameters of particles, the friction coefficients, and the fluid rheology are the same as Case *2*.

Figure *4-16 (a)* shows the proppant distribution in the primary fracture in Case *2* and *Figure 4-16 (b)* shows the proppant distribution in the primary fracture in Case *3*. In both cases, the maximum height of the proppant dune is located at the intersection of the fractures. The major difference in the two cases is the value of the maximum height of the proppant dune. As the designed fracture height of Case *3* is only half the height in Case *1*, the maximum equilibrium height of the proppant dune in Case *3* is lower than Case *1*.

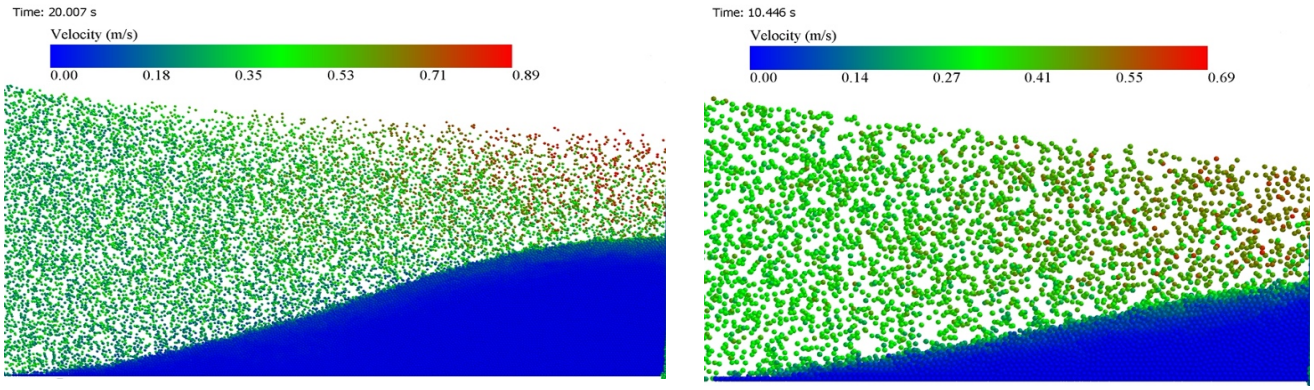

(a) **(b)**

Figure **4-16**: Comparison of proppant distribution in primary fracture of Case *2* and Case *3*

Figure 4-17 (a) shows the proppant distribution of the secondary fracture in Case *1* and *Figure 4-17 (b)* shows the proppant distribution of the secondary fracture in Case *3*. The proppant distributions in the secondary fractures among the two cases are similar, and the maximum height of the proppant dune is located in the middle of the fractures. In both cases, the secondary

fracture has a higher proppant dune equilibrium height than the primary fractures. In Case *3*, the sand dune's maximum equilibrium height in the primary fracture is *18 mm*, which is *36*% of the designed fracture height. The sand dune's maximum equilibrium height in the secondary fracture is *27 mm*, which is *54*% of the designed fracture height. As noted previously, in Case *2* the maximum equilibrium height of the sand dune in the primary fracture is *43 mm*, which is *43*% of the designed fracture height, and the sand dune's maximum equilibrium height in the secondary fracture is *62 mm*, which is *62*% of the designed fracture height, meaning a difference of about *8*% can be identified between the two cases, which can be translated into the same amount of changes in fractures' conductivity.

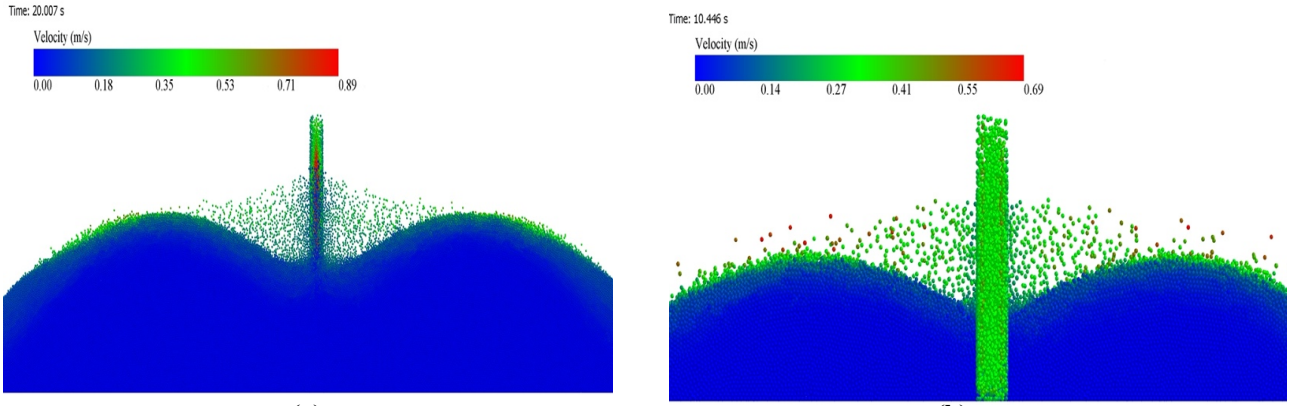

(a) **(b)**

Figure **4-17**: Comparison of proppant distribution in secondary fracture of Case 2 and Case *3*

Figure 4-18 shows the number of proppants inside the fracture system during the simulation. The solid lines in the figure indicate the slope change. As introduced in the previous case, the proppant dune in the primary fracture reaches equilibrium height at *3.8 s*, after injecting *12.73* primary fracture volumes of proppant slurry. The proppant dune in the secondary fracture reaches an equilibrium height at *7.8 s*, after injecting *26.13* primary fracture volumes of proppant slurry. As the scale of time T equals L/V, since the scale of length L has reduced two times, the

scale of time would reduce two times as well. Then, an operation time of *3.8 s* and *7.8 s* in Case *3* would equal an operation time of *7.6 s* and *15.6 s* in Case *2*.

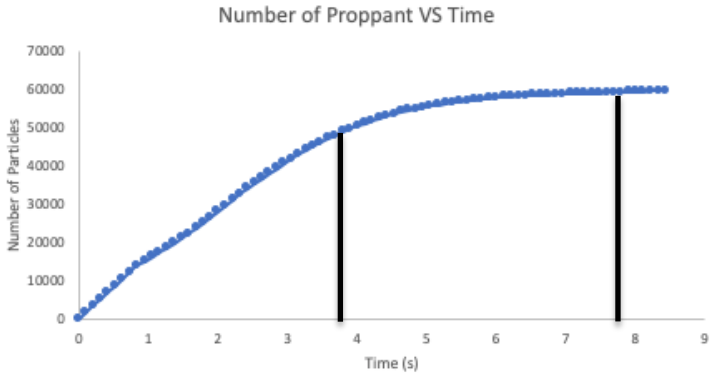

Figure **4-18**: Number of proppants in fracture during the simulation of Case *3*

Previous researchers have also performed experiments on T-shaped fracture networks. Among those, the experiment performed by Sahai *et al*. (2014) is one of the most recognized. A T-shaped fracture network was introduced in their lab experiment to study proppant displacement in the fracture network. To further verify the accuracy of the numerical simulation model, a comparison was performed. The T-shaped fracture network in their experiment was called the "T*2*" fracture slot, the schematic diagram of which is shown in *Figure 4-19*. The experiment uses a proppant size of *30/70* mesh with a pumping rate of *15.4 gal/min*. The concentration of the proppant slurry equals *0.46 lb./gal*. The length to height ratio of the primary fracture is *0.5*, and the length to height ratio of the secondary fractures is *2*.

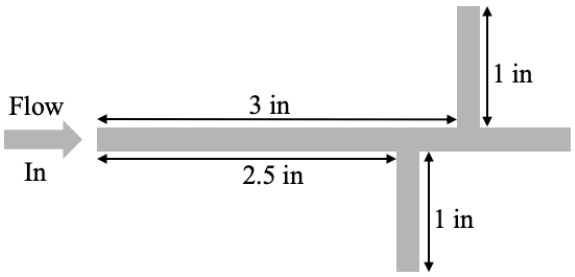

Figure **4-19**: Schematic Diagram of T*2* Slot

Figure 4-20 shows a comparison between simulation results and lab experiment results of the primary fracture and shows that the results are consistent in the overall proppant distribution, as the shape and the position of the deposited sand dune are the same. However, the maximum height of the sand dune is located near the intersection of the fracture in the simulation, and the maximum height in the lab experiment is located at the end of the fracture. This difference is caused by the different designs of the T-shaped fractures between the numerical work and lab experiments. Moreover, due to the difference in some key factors, such as the proppant material, the overall slope of the sand dune is different between the two results. *Figure 4-21* shows a comparison between the simulation results and lab experiment results of the secondary fracture. In both, the maximum height of the sand dune in the secondary fracture is in the middle of the secondary fracture; however, since the secondary fracture half-wings are located in the middle of the primary fracture in the experiment, the full impact of the secondary fractures on proppant distribution in the primary fracture cannot be further compared.

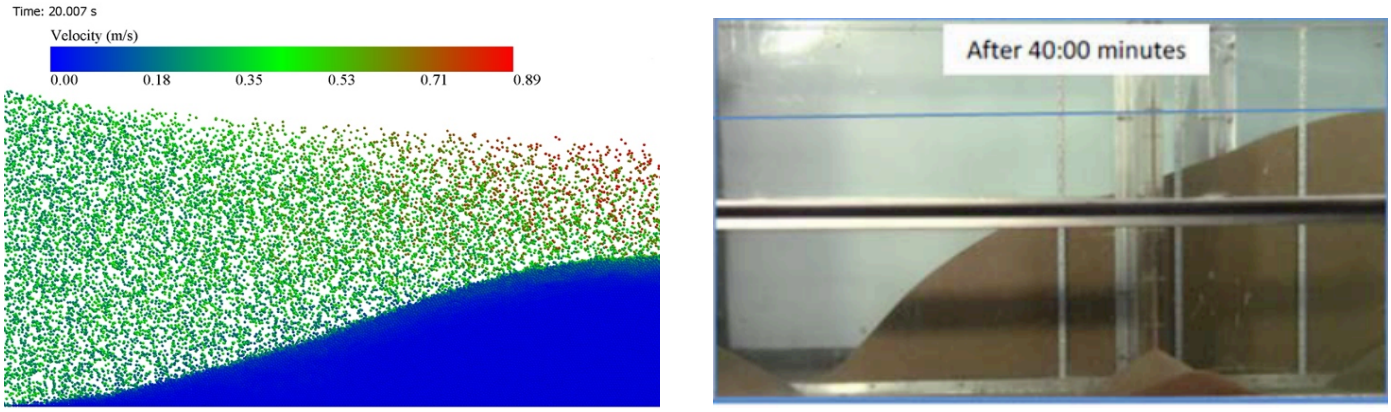

(a) **(b)**

Figure **4-20**: Comparison of simulation result and lab experiment result of primary fracture

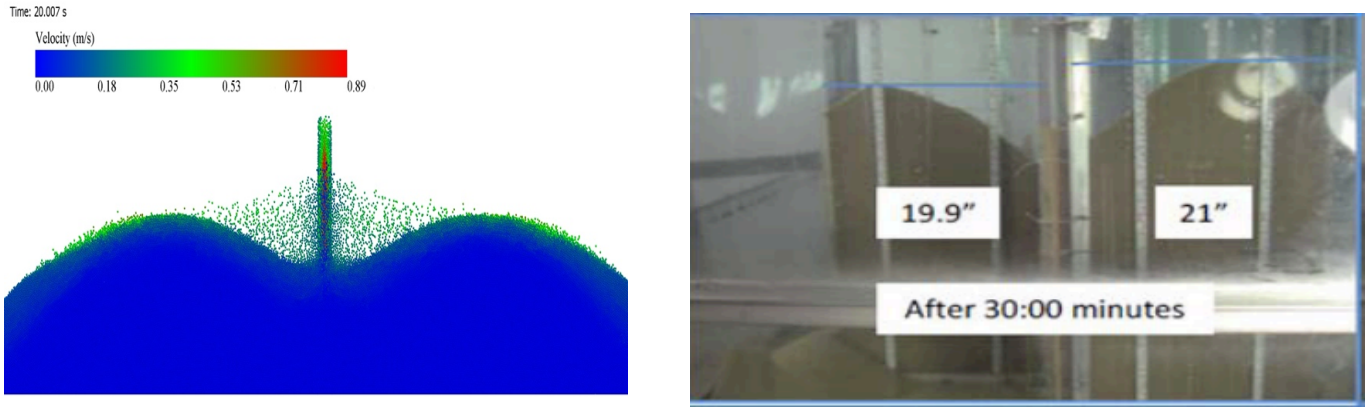

(a) **(b)**

Figure **4-21**: Comparison of simulation result and lab experiment result of secondary fracture

Case 4: Impact of the Bypass Fracture

When performing a hydraulic fracturing treatment, the natural fracture would significantly impact on the shape of the fracture network. As the length and the direction of natural fractures are uncertain, they could connect to the cracked fracturing as a bypass fracture. In this case, a T-shaped fracture network was introduced into the simulation. In contrast to previous cases, a bypass fracture

was set as the secondary fracture to determine the impact of the bypass fracture. In Case *4*, the geometry model and mesh strategy are the same as Case *2*; however, in Case *4*, the inlet from Case *2* would be set as an outlet, and the outlet would set as the inlet. In other words, the secondary fracture in Case *2* would act as the primary fracture in Case *4*, and the primary fracture in Case *2* would be set as the bypass fracture in Case *4*.

The particles are generated in the DEM simulation at the fixed rate of *33567* particles per second and are allocated random positions at the inlet cross-section. The load of the proppant slurry is assumed to be *0.4 lb./gal*. The physical parameters of the particles, the friction coefficients, and the fluid rheology are the same as in the previous case. The boundary conditions for CFD simulations are the same as the previous cases.

Figure 4-22 shows the proppant distribution in the primary fracture of Case *4* after injecting *57.75* primary fracture volumes of proppant slurry. The proppants transport into the primary fracture first and then flow further into the bypass fracture. After injecting *3.3* primary fracture volumes of the proppant slurry, proppants started to deposit around the intersection and gradually formed a sand dune. The maximum height of the sand dune is located around the intersection and keeps moving forward. After the maximum height of the dune passes the intersection of the fracture network, the majority of the injected proppants start to deposit near the outlet. The sand dune's maximum equilibrium height in the primary fracture is located near the outlet with a height of *65 mm*, which is *65*% of the designed fracture height. *Figure 4-23* shows the proppant distribution in the bypass fracture of Case *4*. The proppants start to settle around the intersection and continue moving. The maximum height of the deposited proppant dune is located at the intersection. The maximum equilibrium height of the sand dune is *56 mm*, which is *56*% of the designed fracture height. In contrast to the previous cases, the growth rate of the sand dunes is the same in both the primary and bypass fractures. The sand dunes reach equilibrium height at the

same time as well. The whole system reaches equilibrium height *26* s after injecting *42.9* primary fracture volumes of proppant slurry into the simulation.

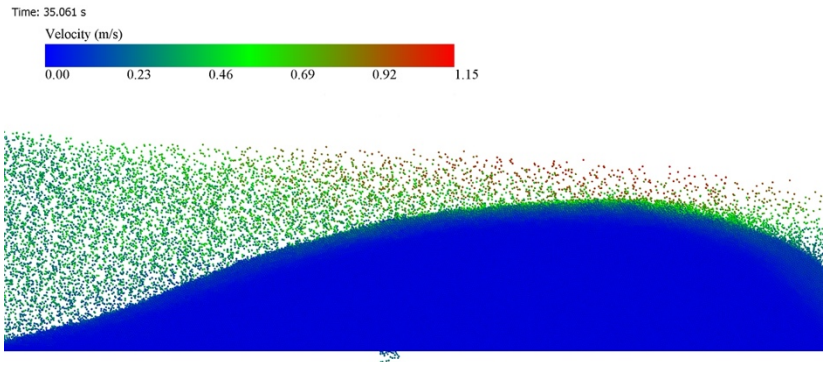

Figure **4-22**: Proppant distribution in the primary fracture of Case *4*

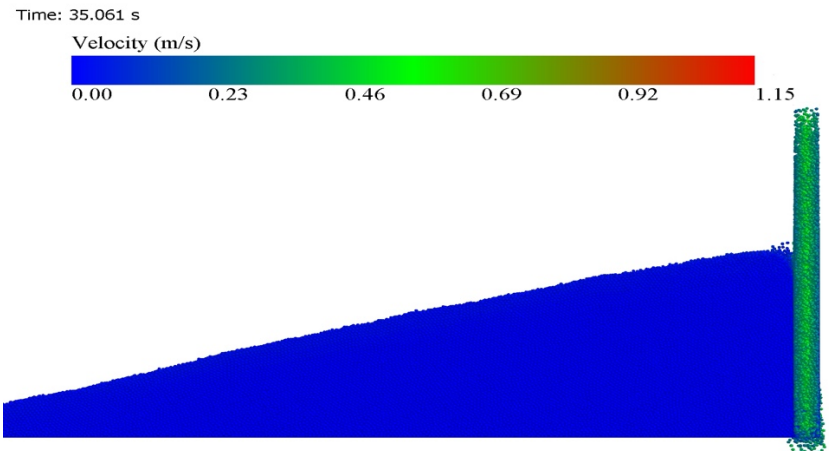

Figure **4-23**: Proppant distribution in the bypass Fracture of Case *4*

Figure 4-24 (a) shows the plot of the outflow velocity vs. flow time in the primary fracture. As the proppant slurry flows into the primary fracture, the outflow velocity increases gradually. The overall velocity is less than the injection velocity at an earlier stage, and then, as the sand dune moves deeper, the velocity matches the injection velocity. After the sand dune reaches equilibrium height, the velocity tends to be constant. *Figure 4-24 (b)* shows the plot of the outflow velocity vs. flow time in the bypass fracture. The outflow velocity of the bypass fracture is much smaller than the primary fracture. As the fracturing fluid flowed into the bypass fracture without the effect of

the proppant, the outflow velocity increased. Then, as the proppants began to move and deposit into the fracture, the outflow velocity continued to decrease. When more proppants settled, the outflow velocity began to increase and kept a relatively constant value after the overall system reached equilibrium. A significant velocity change was identified at the first *7.5* seconds of the simulation, after injecting *12.375* primary fracture volumes of proppant slurry. A similar change could also be observed in the plot of total particle numbers vs. simulation time. Within the plot, the increased rate of particles in the fractures has a significant change at *7.5 s*. When looking into the proppant displacement behavior during that period, the changes result from the change of deposit mechanism of proppants in the bypass fracture.

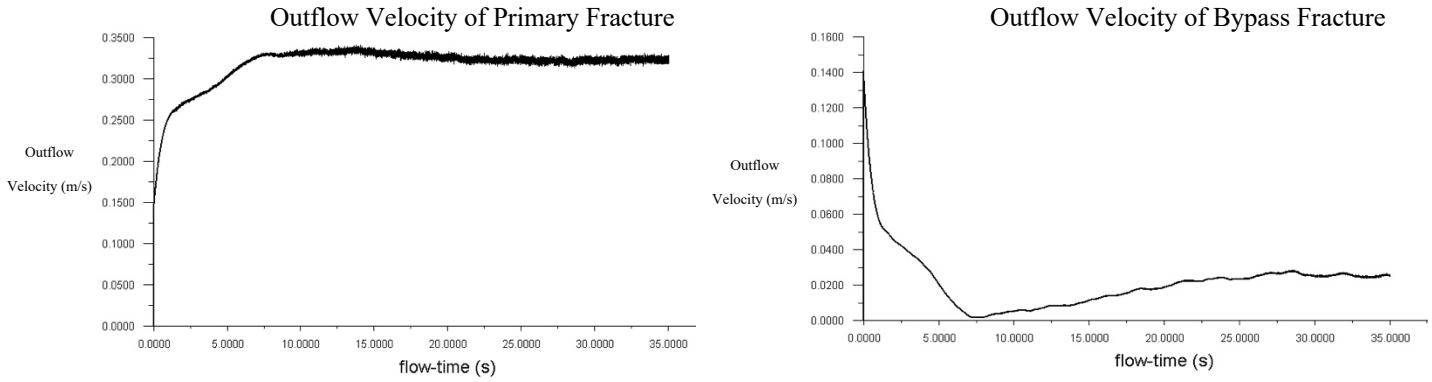

(a) **(b)**

Figure **4-24**: Outflow velocity of Case *4*

Figure 4-25 (a) shows the deposit mechanism up to *7.5 s* of the simulation, and *Figure 4-25 (b)* shows the deposit mechanism after *7.5 s*. During the first *7.5 s*, only a few proppants move into the bypass fracture and fall to the bottom of the fracture, mainly as the result of gravity. Meanwhile, an energy loss of the fracturing fluid has occurred to compensate for the impact of gravity on the proppant particles. As a result, the outflow velocity continues to decrease. After *7.5 s*, since the velocity is low and is not able to compensate for gravity, the newly injected proppants

start rolling into the bypass fracture through the surface of the existing proppant dune. The dominant force for this deposit is the friction among proppant particles.

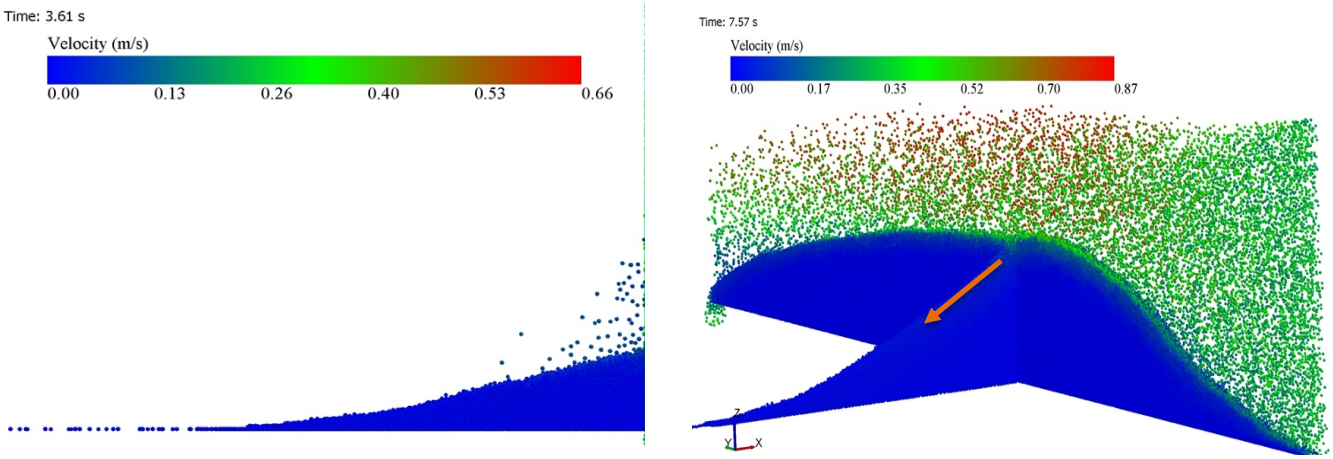

Figure **4-25**: Comparison of deposit mechanism of proppant in bypass fracture

Figure 4-26 shows the interaction between fluid and particles in Case *4*. Similar to previous cases, a high-velocity zone could be identified. A higher sand dune would cause higher velocity, but the velocity profile in the bypass fracture is different from other cases and the velocity in the bypass fracture is lower than the velocity in the primary fracture. A higher sand dune would not lead to a high-velocity zone. The difference between the two fractures in Case *4* results from the injection direction. A significant energy loss occurs as the fluid around the intersection needs to change the direction to about *90* degrees to flow into the bypass fracture.

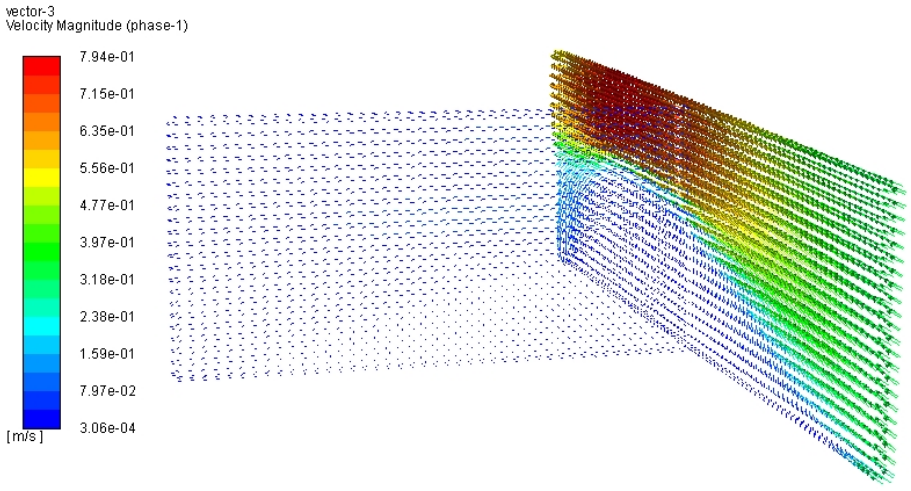

Figure **4-26**: Interaction between fluid and particles of Case *4*

Case 5: Impact of Proppant Concentration

In the previous study, one of the most critical parameters that impacted proppant distribution was proppant concentration. The concentration of the proppant slurry impacts on the total number of particles that participate in the proppant transport process as well as the interaction between fracturing fluid and proppant particles. This case aims to determine the impact of proppant concentration on proppant displacement. The geometry model and mesh strategy of Case *5* are the same as Case *2*.

The particles are generated in the DEM simulation at the fixed rate of *16783* particles per second and are allocated random positions at the inlet cross-section. The load of the proppant slurry is assumed to be *0.2 lb./gal*. The initial velocity of each particle is *0.33 m/s*. The physical parameters of particles, the friction coefficients, and the fluid rheology are the same as in the previous case. The boundary conditions for CFD simulations are the same as in the previous cases.

Figure 4-27 (a) shows proppant distribution in the primary fracture, and *Figure 4-27 (b)* shows proppant distribution in the secondary fracture. The shape of this proppant dune is similar to Case *2*. The maximum height of the proppant dune in the primary fracture is located at the intersection of the fracture network, and the maximum height of the proppant dune in the secondary fracture is located in the middle of the fracture. However, the deposit processes in the two cases are different. With a lower concentration, the impact of the proppant dune formed in the primary fracture was mitigated. The efficiency of the fracturing fluid transport is improved, and more particles were transported into the secondary fracture. Consistent with Case *2*, the proppant dune in the secondary fracture reaches equilibrium after the dune in the primary fracture reaches equilibrium, but the whole proppant system in Case *5* needs longer to reach equilibrium. In Case *5*, the proppant dune in the primary fracture reaches equilibrium height at *12 s*, and the proppant dune in the secondary fracture reaches equilibrium at *19 s*. In addition, the maximum equilibrium height of the proppant dune in the primary fracture is *33 mm*, which is *33*% of the designed fracture height, and the maximum height in the secondary fracture is *52 mm*, which is *52*% of the designed fracture height. The final equilibrium height is shorter than the height in Case *2* but is similar to the height in Case *3*. When comparing the three cases, Case *1* has a higher proppant concentration with the same geometry scale, while Case *3* has a higher proppant concentration but has a smaller geometry scale. This might indicate that the final equilibrium height is not decided by the fracture scale or proppant concentration but by the total amount of the proppant per second that was injected into the fracture.

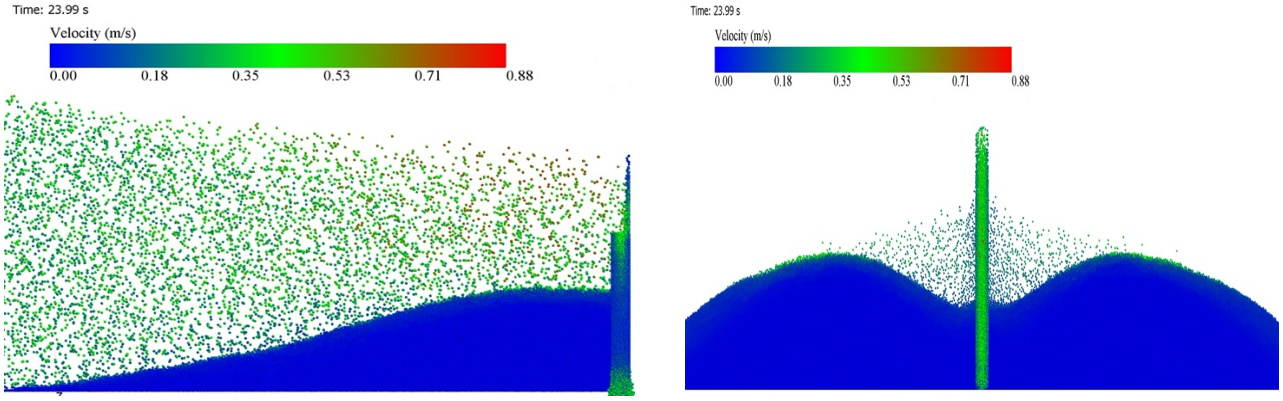

(a) **(b)**

Figure **4-27**: Proppant distribution in fracture network of Case *5* with lower concentration

To further study the impact of proppant concentration, another simulation with a higher proppant concentration was performed in Case *5*. The dimensions of the geometry model in this case are the same as in Case *2* and the mesh for this case is generated under the same meshing strategy as Case *2*. The particles are generated in the DEM simulation at the fixed rate of *50350* particles per second and are allocated random positions at the inlet cross-section. The load of the proppant slurry is assumed to be *0.2 lb./gal*. The initial velocity of each particle is *0.33 m/s.*

Figure 4-28 (a) shows proppant distribution in the primary fracture, and *Figure 4-28 (b)* shows proppant distribution in the secondary fracture, showing a proppant distribution similar to Case *2*. The maximum height of the proppant dune in the primary fracture is located at the intersection of the fracture, and the maximum height of the dune in the secondary fracture is located at the middle. The sand dune in the primary fracture reaches equilibrium at *6 s*, after injecting *10.05* primary fracture volumes of proppant slurry. The maximum equilibrium height of the dune is *56 mm*, which is *56*% of the designed fracture height. The sand dune in the secondary fracture reaches equilibrium at *12 s*, after injecting *20.1* primary fracture volumes of proppant slurry. The maximum equilibrium height of the dune is *71 mm*, which is *71*% of the designed fracture height.

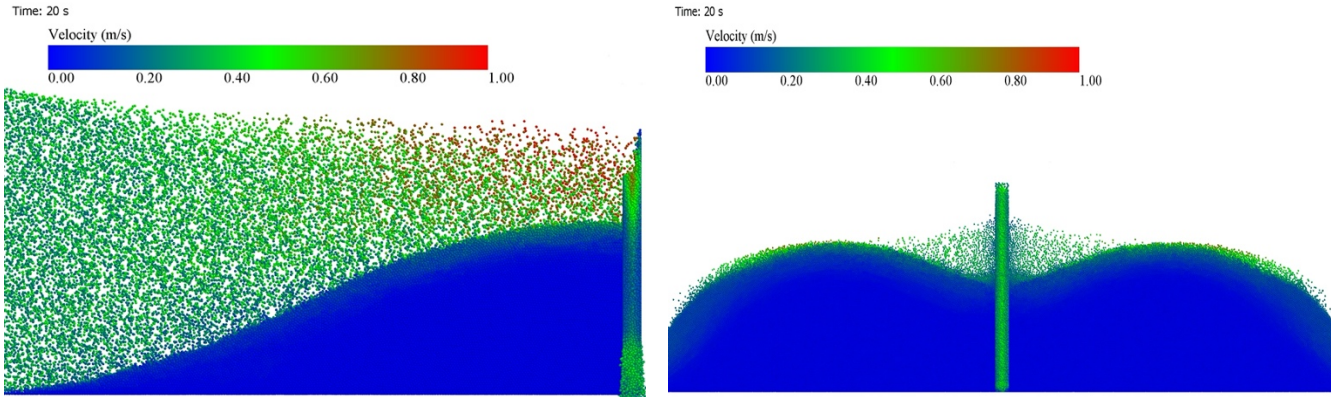

(a) **(b)**

Figure **4-28**: Proppant distribution in fracture network of Case *5* with higher concentration

As the proppant concentration changes from *0.2 lb./gal* to *0.6 lb./gal*, the maximum equilibrium height of the sand dune changes as well, from *33 mm* to *52 mm* in the primary fracture, and from *52 mm* to *71 mm* in the secondary fracture. Increasing the proppant concentration by *50*% of proppant concentration, the maximum height would increase by about *10*% of the designed fracture height. The result also shows that the concentration has a major impact on the sand dune's equilibrium height but a minor impact on the overall distribution of the proppants. A higher proppant concentration would reduce the time needed for the proppant dune to reach equilibrium.

Case 6: Impact of Proppant Mesh Size

In practical field applications, proppant size can vary from *100/120* mesh size to *10/20* mesh size. The size of proppants can be even larger in some specific cases such as fracpack applications. Previous studies have mainly focused on the impact of proppant size on equilibrium height or overall distribution of particles. In recent years, although the concept of injecting several sizes of proppant particles at the same stage was introduced into the industry under different trademarks, numerical simulation work on this concept is still insufficient. The new simulation

approach performed here can be utilized to study these features on the transportation performance of proppant particles.

The dimensions of the model, we considered to study this impact, is the same as in Case *2*. The particles are generated and allocated random positions at the inlet cross-section. Three sizes of proppant were introduced into the simulation: *10* mesh size, *20* mesh size, and *40* mesh size. The mass of each type of particle is kept the same, and the initial velocity for each particle is set to *0.33 m/s*. The physical parameters of particles, the friction coefficients, and the fluid rheology are the same as in the previous case.

During the earlier stages of the Case *6* simulation, smaller particles were transported farther into the secondary fracture and settled as the base of the sand bed. The medium- and large-size particles began to deposit near the inlet of the primary fracture and increase the height of the sand dune. That may explain why fine proppants (like mesh *100*) could be a better solution for propping complex fracture networks in shales. *Figure 4-29 (a)* shows the proppant distribution in the primary fracture. In the primary fracture, the proppants began to settle at the inlet of the fracture. The three sizes of particles mixed well and formed a proppant dune. The smaller-sized proppants usually settled at the bottom of the proppant dune and formed the majority of the dune, whereas the medium-size proppants usually settled in the middle of the dune. Although large-size proppants can be distributed throughout the proppant dune, there is a higher concentration on the surface. The sand dune in the primary fracture has a higher increase rate as most large-size particles are deposited in the primary fracture. *Figure 4-29 (b)* shows the proppant distribution in the secondary fracture in which the proppant dune is primarily formed by small- and medium-sized proppants. In the middle of the figure is the proppant deposited in the primary fracture. Since the large-sized proppants are heavier in weight and larger in diameter compared to the other two sizes, they are less likely to be transported into the secondary fracture. In this case, the height of the proppant dune in the secondary fracture is much shorter than in the primary fracture. As the dune formed near the

inlet, this would impede proppants injected in later stages from moving farther, thus, due to the reduced numbers of injected particles in secondary fracture, the sand dune would not be as high as the dune in the other cases.

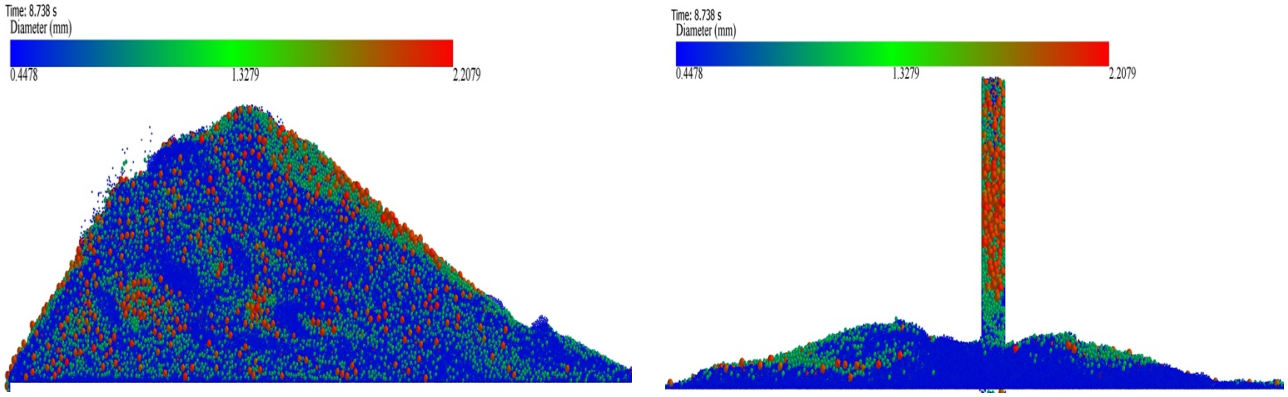

(a) **(b)**

Figure **4-29**: Proppant distribution in fracture network of Case *6*

Case 7: Impact of Injection Velocity

In the proppant transport process, injection velocity has a major impact on the final distribution of the proppants because the injection velocity is related to the forces applied to the particles by the fluid phase. The forces provided by the fluid can have a significant effect on the motion of the proppant particles as proppant transport is a multiphase flow. Thus, it is crucial to recognize how injection velocity could affect the final distribution of the proppants; therefore Case *7* aims to identify the impact of injection velocity.

The dimensions of the geometry model in this case are the same as in Case *2*. The length of the fracture is *0.2 m*, and the height of the fracture is *0.1 m*. Mesh for this case is generated under the same meshing strategy as Case *1*. The particles are generated in the DEM simulation at the fixed rate of *24575* particles per second and are allocated random positions at the inlet cross-section.

The load of the proppant slurry is assumed to be *0.4 lb./gal*. The initial velocity of each particle is *0.22 m/s*. The physical parameters of particles, the friction coefficients, and the fluid rheology are the same as in the previous case. The boundary conditions for CFD simulations have been defined in a such a way that at the inlet the velocity is kept constant at *0.22 m/s*. As for the outlets, the pressure is assumed to be equal to the reservoir pressure, or zero net pressure.

Figure 4-30 (a) shows the early stages of proppant distribution in the primary fracture. After injecting *11.94* primary fracture volumes of proppant slurry, the overall shape of the proppant dune is the same as in Case *2,* but there are other differences. With a lower injection velocity, the injected proppants in Case *7* deposit mainly around the middle of the fracture due to a smaller drag force applied on them. After most of the proppants settled in the middle of the primary fracture, the whole dune moves slowly toward the secondary fracture. The highest part of the sand dune is located in the middle of the fracture. *Figure 4-30 (b)* shows proppant distribution in the secondary fracture after injecting *7.96* primary fracture volumes of proppant slurry. Proppants start to settle at the intersection after injecting *4.46* primary fracture volumes of proppant slurry. The highest part of the sand dune is located at the intersection.

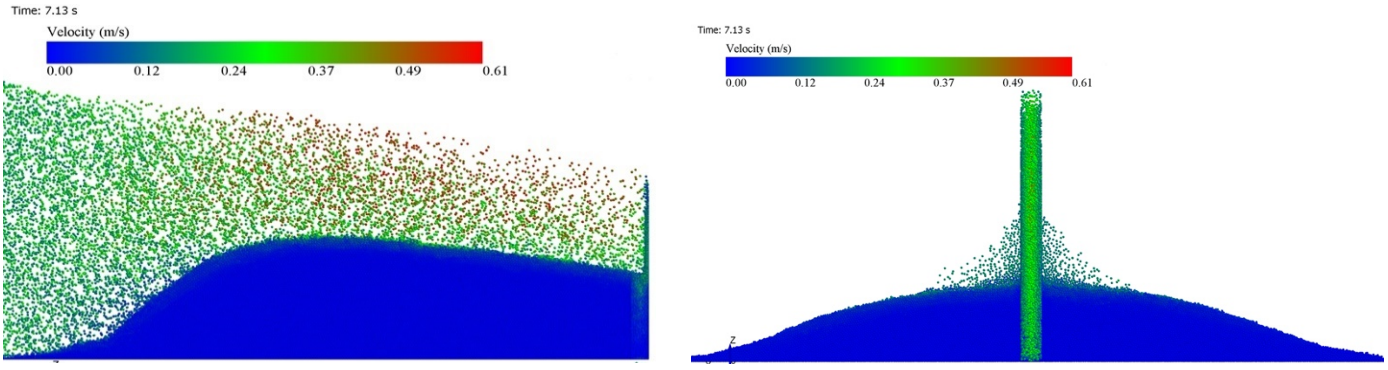

(a) **(b)**

Figure **4-30**: Proppant distribution after injecting *7.96* primary fracture volumes proppant slurry of Case *7* with injection rate as *0.22 m/*s

Figure 4-31 (a) shows proppant distribution in the primary fracture after injecting *69.25* primary fracture volumes of proppant slurry. The sand dune that developed in an earlier stage has now been transported farther into the secondary fracture. As more proppants settle, a flat surface on the sand dune can be observed. The highest part of the sand dune has also moved to the intersection of the fractures, which is consistent with the results obtained in Case *2*. *Figure 4-31 (b)* shows proppant distribution in the secondary fracture in the later stages. After injecting *69.25* primary fracture volumes of proppant slurry, the maximum height of the proppant dune moves to the middle of the fracture. The sand dune's maximum equilibrium height in the primary fracture is *61 mm*, which is *61*% of the designed fracture height. The sand dune in the primary fracture reaches equilibrium height at *15 s*. The sand dune's maximum equilibrium height in the secondary fracture is *63 mm*, which is *63*% of the designed fracture height. The sand dune in the secondary fracture reaches equilibrium height at *20 s*. The equilibrium height of the sand dune in the secondary fracture is similar to the height in Case *2.* Also, the equilibrium height of the sand dune in the secondary fracture is higher than that of the primary fracture. However, Case *7* has higher equilibrium heights. Moreover, the difference between the equilibrium height of the sand dune in the primary and secondary fractures in Case *7* is negligible, whereas in Case *2* the difference is *19 mm*. Case *7* takes longer than Case *2* to reach equilibrium height. The additional time required to reach equilibrium results mainly from the sand dune in the primary fracture, which needs *7.5 s* more to reach equilibrium height. Thus, the impact of injection velocity is performed mainly on the primary fracture. Also, as the drag force has reduced, more proppant could settle in the primary fracture and lead to an incremental increase in sand dune height.

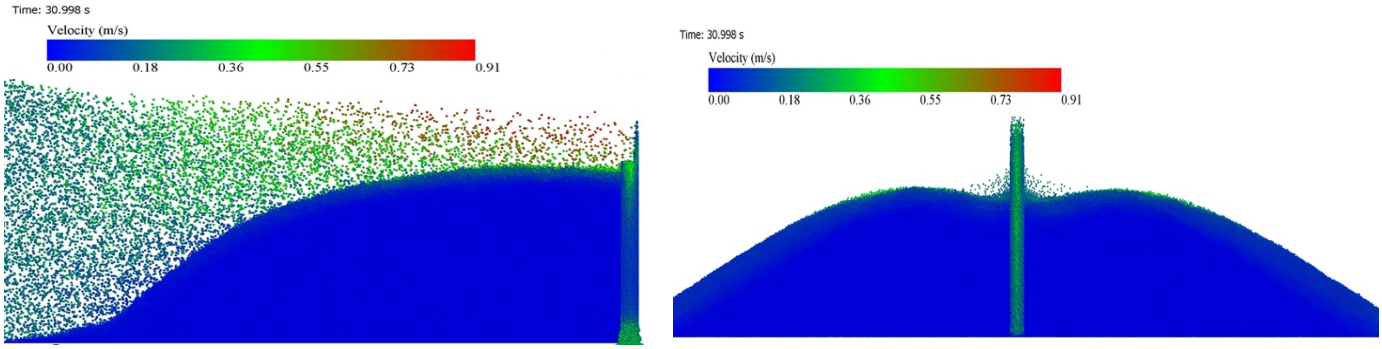

(a) **(b)**

Figure **4-31**: Proppant distribution after injecting *69.25* primary fracture volumes proppant slurry of Case *7* with injection rate as *0.22 m/*s

To further study the impact of injection velocity, another simulation with a higher injection velocity was performed in Case *7*. The dimensions of the geometry model in this case are the same as in Case *2*. The mesh for this case was generated under the same meshing strategy as Case *2,* as well.

The particles are generated in the DEM simulation at the fixed rate of *44756* particles per second and are allocated random positions at the inlet cross-section. The load of the proppant slurry is assumed to be *0.4 lb./gal*. The initial velocity of each particle is *0.44 m/s*. The physical parameters of particles, the friction coefficients, and the fluid rheology are the same as in the previous case. The boundary conditions for CFD simulations have been defined in a such a way that at the inlet, the velocity is kept constant at *0.44 m/s*. As for the outlets, the pressure is assumed to be equal to the reservoir pressure, or zero net pressure.

Figure 4-32 (a) shows proppant distribution in the primary fracture. From the primary fracture, the proppants could move further into the secondary fracture. The deposit process has been slowed down due to the high transport velocity. The overall proppant distribution in this simulation is similar to the results obtained in Case *3*. The maximum height of the sand dune is

located at the intersection. *Figure 4-32 (b)* shows proppant distribution in the secondary fracture. In the secondary fracture, the majority of the sand dune had developed in an earlier stage. The maximum height of the sand dune is located in the middle of the fracture. Different from previous cases, the sand dune in the primary fracture reaches equilibrium height after the sand dune in the secondary fracture reaches its equilibrium. The equilibrium height of the sand dune in the primary fracture is shorter than in the previous cases. The sand dune's maximum equilibrium height is *27 mm*, which is *27*% of the designed fracture height. The sand dune in the primary fracture reaches equilibrium height at *10 s*. The sand dune's maximum equilibrium height in the secondary fracture is 56 *mm*, which is *63*% of the designed fracture height. The sand dune in the secondary fracture reaches equilibrium height at *5 s*. This indicates that a higher injection velocity enhances the transport capacity of the fluid, and more proppants would therefore be transported into the secondary fracture as the majority of proppants first deposit in the secondary fracture rather than in the primary fracture. As a result, the sand dune in the secondary fracture reaches equilibrium height first, and the maximum height of the dune is moved farther into the middle of the fracture. A higher injection velocity also provides a higher drag force on particles, which reduces the equilibrium height of the sand dunes.

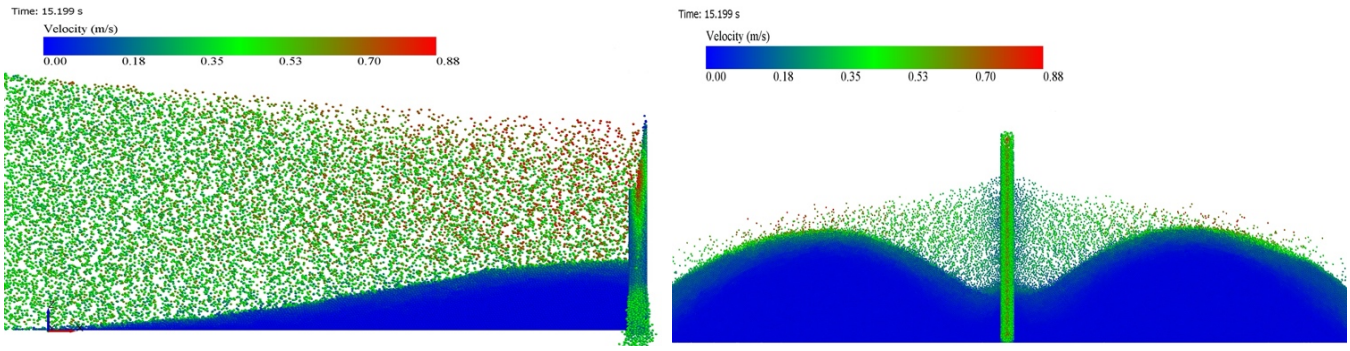

(a) **(b)**

Figure **4-32**: Proppant distribution of Case *7* with injection rate as *0.44 m/s*

As proppant injection velocity increases from *0.22 m/s* to *0.44 m/s*, the maximum equilibrium height of the sand dune changes due to proppant erosion at higher velocities. The maximum height changes from *61 mm* to *27 mm* in the primary fracture, and from *63 mm* to *56 mm* in the secondary fracture. Increasing the injecting velocity by *50*%, the maximum height of sand dune in the primary fracture would decrease by about *34*% of the designed fracture height. The height of the secondary fracture is reduced by *7*% of the designed fracture height, showing that the injection velocity has a major impact on the sand dune's equilibrium height in the primary fracture but only a minor impact on the height in the secondary fracture.

Chapter 5

Conclusions

While existing CFD-DEM models assume that the particle phase is as continuous as the fluid phase, we developed a coupled fluid flow and discrete particle model to identify and track the interactions between particles. A scaling analysis was introduced into the modeling process, and several dimensionless parameters were selected from a previous study. Instead of using the field scale to initiate the model, proppant transport simulation was achieved by keeping the dimensionless parameters constant in a scaled fracture network. The scaled model reduces the required computational time and enhances the efficiency of the simulation. Following are the specific conclusions drawn from this work.

From the simulation results, three zones for injected proppants were identified based on the motion/settlement of the injected proppant: slurry flow zone, surface rolling zone, and sand bed zone. The dominant force in the slurry flow zone is the drag force from the fracturing fluid, whereas the dominant force in the sand bed zone is the friction between particles.

It has noticed that different fracture configuration and fluid system has reached an equilibrium point. Several signs indicate equilibrium of the sand dune, including constant outflow velocity and injection pressure. Due to the impact of the proppant dune, a high-velocity zone can be identified above the sand dune surface. The majority of this zone is located in the slurry flow zone. The simulation results indicate that the velocity of the fluid is closely related to the height of the proppant dune: a higher proppant height could produce a higher fluid flow velocity.

Proppants start to settle at the inlet of the fracture in the absence of secondary fracture. When a secondary fracture is introduced into the model, the proppants will settle at the intersection due to a low-velocity zone being created by the intersection. When a bypass fracture exists, the

sand dunes in both fractures share a uniform growth rate and reach equilibrium at the same time. Two deposition mechanisms were identified: falling deposition is dominated by gravity; and the rolling deposition is dominated by friction. Changes in the deposition mechanism may lead to changes in outflow velocity. The injection velocity has a major impact on proppant distribution in the primary fracture. A lower injection velocity would increase the time required for the primary fracture to reach equilibrium which mitigates the difference of the equilibrium height of the sand dunes in primary and secondary fractures. A higher injection velocity would increase the fluid's carrying capacity and reduce the equilibrium height of the sand dune.

Large-size proppants increase the height of the sand dune, whereas smaller proppants increase the length of the dune. One may relate this phenomenon to the transportability of particles in different sizes, as smaller particles could be transported further, whereas larger particles trend to deposit around the inlet.

References

Alotaibi, M. A., & Miskimins, J. L. (2015). Slickwater proppant transport in hydraulic fractures: New experimental findings and scalable correlation. *SPE Production and Operations*, *33*(2), 164–178. https://doi.org/10.2118/174828-pa

Barree, R. D., & Conway, M. W. (1995). Experimental and numerical modeling of convective proppant transport. *JPT, Journal of Petroleum Technology*, *47*(3), 216–222. https://doi.org/10.2523/28564-ms

Brannon, H. D., Wood, W. D., & Wheeler, R. S. (2006). Large-scale laboratory investigation of the effects of proppant and fracturing-fluid properties on transport. *Proceedings - SPE International Symposium on Formation Damage Control*, *2006*, 19–31. https://doi.org/10.2523/98005-ms

Britt, L. K., Smith, M. B., Haddad, Z., Lawrence, P., Chipperfield, S., & Hellman, T. (2006). Water-fracs: We do need proppant after all. *Proceedings - SPE Annual Technical Conference and Exhibition*, *2*, 1370–1384. https://doi.org/10.2523/102227-ms

D.E.M. Solutions. (2018). Simulator. *EDEM 2018 User Guide–Creator, DEM Solutions Ltd., Edinburgh, United Kingdom*.

Dahi Taleghani, A., Gonzalez-Chavez, M., Yu, H., & Asala, H. (2018). Numerical simulation of hydraulic fracture propagation in naturally fractured formations using the cohesive zone model. *Journal of Petroleum Science and Engineering*, *165*(February), 42–57. https://doi.org/10.1016/j.petrol.2018.01.063

Fernández, M. E., Sánchez, M., & Pugnaloni, L. A. (2019). Proppant transport in a scaled vertical planar fracture: Vorticity and dune placement. *Journal of Petroleum Science and*

Engineering, *173*(July 2018), 1382–1389. https://doi.org/10.1016/j.petrol.2018.10.007

Gadde, P. B., Liu, Y., Norman, J., Bonnecaze, R., & Sharma, M. M. (2004). Modeling proppant settling in water-fracs. *Proceedings - SPE Annual Technical Conference and Exhibition*, 373–382. https://doi.org/10.2523/89875-ms

Gidaspow, D. (1994). *Multiphase Flow and Fluidization: Continuum and Kinetic Theory Descriptions*. Academic Press.

He, Y., Bayly, A. E., & Hassanpour, A. (2018). Coupling CFD-DEM with dynamic meshing: A new approach for fluid-structure interaction in particle-fluid flows. *Powder Technology*, *325*, 620–631. https://doi.org/10.1016/j.powtec.2017.11.045

J. G. Santiago. (2019). *A first course on Dimensional analysis*.

Jordan. (2013). Bed load proppant transport during slickwater hydraulic fracturing: insights from comparisons between published laboratory data and correlations for sediment and pipeline slurry transport. *Journal of Chemical Information and Modeling*, *53*(9), 1689–1699. https://doi.org/10.1017/CBO9781107415324.004

Kern, L. R., Perkins, T. K., & Wyant, R. E. (1959). The Mechanics of Sand Movement in Fracturing. *Journal of Petroleum Technology*, *11*(07), 55–57. https://doi.org/10.2118/1108-g

Khan, K. M., & Bushell, G. (2005). Comment on “rolling friction in the dynamic simulation of sandpile formation.” *Physica A: Statistical Mechanics and Its Applications*, *352*(2–4), 522–524. https://doi.org/10.1016/j.physa.2005.01.019

Liu, Y., & Sharma, M. M. (2005). Effect of fracture width and fluid rheology on proppant settling and retardation: An experimental study. *SPE Annual Technical Conference Proceedings*.

Olaleye, A. K., Shardt, O., Walker, G. M., & Van den Akker, H. E. A. (2019). Pneumatic conveying of cohesive dairy powder: Experiments and CFD-DEM simulations. *Powder Technology*, *357*, 193–213. https://doi.org/10.1016/j.powtec.2019.09.046

Patankar, N. A., Joseph, D. D., Wang, J., Conway, M., & Barree, R. D. (2002). Power law

correlations for sediment transport in pressure driven channel flow. *International Journal of Multiphase Flow*, *28*(3), 1269–1292. https://doi.org/10.1016/S0301-9322(02)00152-0

Puyang, P., Taleghani, A. D., Sarker, B., & Yi, H. (2018). Optimal natural fracture realizations by minimizing least squared errors of distances from microseismic events. *Journal of Applied Geophysics*, *159*, 294–303. https://doi.org/10.1016/j.jappgeo.2018.09.020

Sahai, R., Miskimins, J. L., & Olson, K. E. (2014). Laboratory results of proppant transport in complex fracture systems. *Society of Petroleum Engineers - SPE Hydraulic Fracturing Technology Conference 2014*, 35–60. https://doi.org/10.2118/168579-ms

SAKAGUCHI, H., OZAKI, E., & IGARASHI, T. (1993). Plugging of the Flow of Granular Materials during the Discharge from a Silo. *International Journal of Modern Physics B*, *07*(09n10), 1949–1963. https://doi.org/10.1142/S0217979293002705

Shrivastava, K., & Sharma, M. M. (2018). Proppant transport in complex fracture networks. *Society of Petroleum Engineers - SPE Hydraulic Fracturing Technology Conference and Exhibition 2018, HFTC 2018*, *January*, 23–25. https://doi.org/10.2118/189895-ms

Sierra, L., Sahai, R., & Mayerhofer, M. (2014). Quantification of proppant distribution effect on well productivity and recovery factor of hydraulically fractured unconventional reservoirs. *Society of Petroleum Engineers - SPE Canadian Unconventional Resources Conference 2014*, *1*, 369–383. https://doi.org/10.2118/171594-ms

Tong, S., & Mohanty, K. K. (2016). Proppant transport study in fractures with intersections. *Fuel*, *181*, 463–477. https://doi.org/10.1016/j.fuel.2016.04.144

Wang, J., Joseph, D. D., Patankar, N. A., Conway, M., & Barree, R. D. (2003). Bi-power law correlations for sediment transport in pressure driven channel flows. *International Journal of Multiphase Flow*, *29*(3), 475–494. https://doi.org/10.1016/S0301-9322(02)00152-0

Zhang, G., Li, M., & Gutierrez, M. (2017a). Numerical simulation of proppant distribution in hydraulic fractures in horizontal wells. *Journal of Natural Gas Science and Engineering*, *48*,

157–168. https://doi.org/10.1016/j.jngse.2016.10.043

Zhang, G., Li, M., & Gutierrez, M. (2017b). Simulation of the transport and placement of multi-sized proppant in hydraulic fractures using a coupled CFD-DEM approach. *Advanced Powder Technology*, *28*(7), 1704–1718. https://doi.org/10.1016/j.apt.2017.04.008

Appendix

Scaling Analysis via Ipsen's Method

The analysis is performed using Ipsen's method. The Ipsen's method is first introduced by David Carl Ipsen. The purposed of this method is to derive a functional relationship in terms of nondimensional groups of parameters. The procedure (J. G. Santiago, 2019) can be described as following. First, the key parameters should be identified as well as the dimensions of those parameters. Then, based on the governing equations, hypothesize some functions of interest. Next, a parameter that contain the primary dimension that need to be eliminated should be clarified. Last, by multiple or dividing selected parameter to eliminate the remaining parameters that contains the primary dimension selected. Following the steps above, dimensional analysis below can be performed.

From CFD Momentum conservation for fluid and particle which has been introduced in Chapter 2 as equation 2-14, 2-15 and 2-16, the key parameters can be defined as: $\alpha_s,\ \alpha_f,\ \tau_f,\ \rho_s,\ \rho_f,\ g,\ v_s,\ v_f,\ d_s,\ \mu,\ t$. μ is the viscosity of fluid, t is flowing time and g is gravitational acceleration. The primary dimensions within the key parameters are M, L, T. Then the function of interest can be written as

$$P = f\left(\alpha_s,\ \alpha_f,\ \tau_f,\ \rho_s,\ \rho_f,\ g,\ v_s,\ v_f,\ d_s,\ \mu,\ t\right). \qquad (\mathbf{A-1})$$

The dimension of above parameters is

$$ML^{-1}T^{-2} = f(L^3, L^3, ML^{-1}T^{-2}, ML^{-3}, ML^{-3}, LT^{-2}, LT^{-1}, LT^{-1}, L, ML^{-1}T^{-1}, T) \qquad (\mathbf{A-2})$$

Eliminate L by d_s: multiple or dividing d_s to eliminate (cancel) L, then the function interest would be written as

$$Pd_s = f\left(\frac{\alpha_s}{{d_s}^3}, \frac{\alpha_f}{{d_s}^3}, \tau_f d_s, \rho_s {d_s}^3, \rho_f {d_s}^3, \frac{g}{d_s}, \frac{v_s}{d_s}, \frac{v_f}{d_s}, 1, \mu d_s, t\right). \quad (\mathbf{A-3})$$

Eliminate M by $\rho_s {d_s}^3$: multiple or dividing $\rho_s {d_s}^3$ to eliminate (cancel) M, then the function interest would be written as

$$\frac{P}{\rho_s {d_s}^2} = f\left(\frac{\alpha_s}{{d_s}^3}, \frac{\alpha_f}{{d_s}^3}, \frac{\tau_f d_s}{\rho_s {d_s}^3}, 1, 1, \frac{g}{d_s}, \frac{v_s}{d_s}, \frac{v_f}{d_s}, 1, \frac{\mu}{\rho_s {d_s}^2}, t\right). \quad (\mathbf{A-4})$$

Eliminate T by $\frac{d_s}{v_s}$: multiple or dividing $\frac{d_s}{v_s}$ to eliminate (cancel) T, then the function interest would be written as

$$\frac{P}{\rho_s {v_s}^2} = f\left(\frac{\alpha_s}{{d_s}^3}, \frac{\alpha_f}{{d_s}^3}, \frac{\tau_f}{\rho_s {v_s}^2}, 1, 1, \frac{g d_s}{{v_s}^2}, 1, \frac{v_f}{v_s}, 1, \frac{\mu}{\rho_s d_s v_s}, \frac{v_s}{t d_s}\right). \quad (\mathbf{A-5})$$

Then the following dimensionless parameters can be obtained

$$D_2 = \frac{\alpha_s}{{d_s}^3} \qquad D_3 = \frac{\alpha_f}{{d_f}^3} \qquad D_4 = \frac{\tau_f}{\rho_s {v_s}^2} \qquad D_5 = \frac{g d_s}{{v_s}^2}$$

$$D_6 = \frac{v_f}{v_s} \qquad D_7 = \frac{\mu}{\rho_s d_s v_s} \qquad D_8 = \frac{v_s}{t d_s}$$

From DEM Drag Force and particle interaction force, using the same approach, the following new parameters can be obtained.

From the equations for drag force which can be written as

$$\overrightarrow{F_d} = D_p\left(\overrightarrow{v_f} - \overrightarrow{v_s}\right) m, \quad (\mathbf{A-6})$$

$$D_p = \frac{3}{8 S_g} C_d \frac{2\left|\overrightarrow{v_f} - \overrightarrow{v_s}\right|}{d_s}. \quad (\mathbf{A-7})$$

S_g is specific gravity, m is the mass of particles and C_d is drag coefficient which related to A, fracture surface area.

The key parameters can be defined as: $v_f, v_s, m, d_s, \rho_s, \rho_f, \mu, A$. The primary dimensions within the key parameters are M, L, T. Then the function of interest can be written as

$$F_d = f\left(v_f, v_s, m, d_s,\ \rho_s,\ \rho_f, \mu, A\right). \qquad (\mathbf{A-8})$$

The dimension of above parameters is

$$MLT^{-2} = f(LT^{-2}, LT^{-1}, M, L, ML^{-3}, ML^{-3}, ML^{-1}T^{-1}, L^2). \qquad (\mathbf{A-9})$$

Eliminate L by d_s to e: multiple or dividing d_s to eliminate (cancel) L, then the function interest would be written as

$$\frac{F_d}{d_s} = f\left(\frac{v_s}{d_s}, \frac{v_f}{d_s}, m, 1,\ \rho_s\ {d_s}^3,\ \rho_f\ {d_s}^3, \mu d_s, \frac{A}{{d_s}^2}\right). \qquad (\mathbf{A-10})$$

Eliminate M by m: multiple or dividing m to eliminate (cancel) M, then the function interest would be written as

$$\frac{F_d}{m d_s} = f\left(\frac{v_s}{d_s}, \frac{v_f}{d_s}, 1, 1, \frac{\rho_s\ {d_s}^3}{m}, \frac{\rho_f\ {d_s}^3}{m}, \frac{\mu d_s}{m}, \frac{A}{{d_s}^2}\right). \qquad (\mathbf{A-11})$$

Eliminate T by $\frac{d_s}{v_s}$ to: multiple or dividing $\frac{d_s}{v_s}$ to eliminate (cancel) T, then the function interest would be written as

$$\frac{F_d d_s}{m\ {d_s}^2} = f\left(1, \frac{v_f}{v_s}, 1, 1, \frac{\rho_s\ {d_s}^3}{m}, \frac{\rho_f\ {d_s}^3}{m}, \frac{\mu\ {d_s}^2}{v_s m}, \frac{A}{{d_s}^2}\right). \qquad (\mathbf{A-12})$$

Then the following dimensionless parameters can be obtained

$$D_9 = \frac{\rho_s\ {d_s}^3}{m} \qquad D_{10} = \frac{\mu\ {d_s}^2}{v_s m} \qquad D_{11} = \frac{A}{{d_s}^2}$$

From the equations for friction (He *et al.*, 2018) which can be determined as following

$$F_f = -\alpha_s \nabla P + F_d\ . \qquad (\mathbf{A-13})$$

The key parameters can be defined as: $\alpha_s, P, v_f, v_s, r,\ \rho_s,\ \rho_f, \mu, A$. The primary dimensions within the key parameters are M, L, T. Then the function of interest can be written as

$$F_d = f\left(\alpha_s, P, v_f, v_s, r,\ \rho_s,\ \rho_f, \mu, A\right). \qquad (\mathbf{A-14})$$

The dimension of above parameters is

$$MLT^{-2} = f(L^3, ML^{-1}T^{-2}, LT^{-2}, LT^{-1}, L, ML^{-3}, ML^{-3}, ML^{-1}T^{-1}, L^2). \qquad (\mathbf{A-15})$$

Eliminate L by d_s: multiple or dividing d_s to eliminate (cancel) L, then the function interest would be written as

$$\frac{F_d}{d_s} = f\left(\frac{\alpha_s}{{d_s}^3}, Pd_s, \frac{v_s}{d_s}, \frac{v_f}{d_s}, 1, \rho_s {d_s}^3, \rho_f {d_s}^3, \mu d_s, \frac{A}{{d_s}^2}\right). \qquad \mathbf{(A-16)}$$

Eliminate M by $\rho_s {d_s}^3$: multiple or dividing $\rho_s {d_s}^3$ to eliminate (cancel) M, then the function interest would be written as

$$\frac{F_d}{\rho_s {d_s}^4} = f\left(\frac{\alpha_s}{{d_s}^3}, \frac{P}{\rho_s {d_s}^2}, \frac{v_s}{d_s}, \frac{v_f}{d_s}, 1, 1, \frac{\rho_f}{\rho_s}, \frac{\mu}{\rho_s {d_s}^2}, \frac{A}{{d_s}^2}\right). \qquad \mathbf{(A-17)}$$

Eliminate T by $\rho_s {d_s}^3$: multiple or dividing $\frac{d_s}{v_s}$ to eliminate (cancel) T, then the function interest would be written as

$$\frac{F_d}{\rho_s {d_s}^2 {v_s}^2} = f\left(\frac{\alpha_s}{{d_s}^3}, \frac{P}{\rho_s {v_s}^2}, 1, \frac{v_f}{v_s}, 1, 1, \frac{\rho_f}{\rho_s}, \frac{\mu}{\rho_s d_s v_s}, \frac{A}{{d_s}^2}\right). \qquad \mathbf{(A-18)}$$

Then the following dimensionless parameter can be obtained

$$D_{12} = \frac{P}{\rho_s {v_s}^2}.$$